Diurnal Variability of the Hydrologic Cycle in a General Circulation Model

DAVID A. RANDALL

Department of Atmospheric Science, Colorado State University, Fort Collins, Colorado

HARSHVARDHAN

Department of Earth and Atmospheric Sciences, Purdue University, West Lafayette, Indiana

DONALD A. DAZLICH

Department of Atmospheric Science, Colorado State University, Fort Collins, Colorado

(Manuscript received 5 February 1990, in final form 25 June 1990)

ABSTRACT

This paper presents an analysis of the diurnal and semidiurnal variability of precipitation, evaporation, precipitable water, horizontal moisture flux convergence, cloudiness, and cloud radiative forcing, as simulated by the Colorado State University General Circulation Model (GCM). In broad agreement with observations, the model produces an afternoon precipitation maximum over land in warm rainy regions, such as the tropics and the midlatitude summer continents, and an early morning maximum over the oceans far from land. The statistical significance of these model results is demonstrated using a chi-square test. The observed diurnal variation of temperature in the oceanic tropical middle troposphere is also realistically simulated.

Encouraged by these results, the model was used to investigate the causes of the diurnal cycle of precipitation over the oceans. For this purpose, experiments have been performed with an all-ocean global model. Results show that an oceanic diurnal cycle of precipitation occurs even in the absence of neighboring continents and tends to have a morning maximum. It is generally weaker than observed, however. When the radiative effects of clouds are omitted, the simulated diurnal cycle of precipitation is much weaker but still present, with essentially the same phase.

Several experiments have also been performed with a one-dimensional version of the GCM, in which time-dependent large-scale vertical motion can be prescribed. The results show that even in the absence of any systematic daily variation of the large-scale vertical motion, the model produces a diurnal cycle of precipitation with an amplitude of about 1 mm day^{-1}, and a morning maximum.

Finally, previously published results have been followed up, which show that the diurnal cycle strongly affects the partitioning of precipitation between land and sea. The new analysis is based on comparison of three nondiurnal June–July integrations with three Julys from a multiyear diurnally forced seasonal simulation. The results show major changes in the time-averaged surface energy budget, and much more precipitation in "summer monsoon" regimes when the diurnal cycle is omitted.

1. Introduction

Observations show strong diurnal and semidiurnal oscillations in precipitation, mainly in the tropics and the summer hemisphere (e.g., Hamilton 1981a). These oscillations are most prominent over land (e.g., Wallace 1975; Kousky 1980; Meisner and Arkin 1987), but their oceanic amplitudes are by no means negligible (Kraus 1963; Hudlow 1970; Gray and Jacobson 1977; McGarry and Reed 1978; Reed and Lewis 1980; Reed and Jaffe 1981; Murakami 1983; Albright et al. 1985). Their phases and amplitudes show considerable geographic structure as well as systematic seasonal variations. In particular, precipitation typically has an afternoon or evening maximum over heated land and an early morning maximum over the oceans. The causes and consequences of this daily[1] variability have been the subject of much debate; after decades of research, many basic questions remain unanswered.

Daily oscillations are also observed in many other tropospheric meteorological variables, of course, including the surface fluxes of sensible and latent heat over land (Sellers 1965; Wallace and Hobbs 1977), horizontal winds (Roll 1965; Bonner 1968; Wallace and Hartranft 1969; Wallace and Tadd 1974), large-scale horizontal moisture fluxes (Benton and Estoque 1954; Rasmusson 1967, 1968), large-scale mass di-

Corresponding author address: Dr. David A. Randall, Department of Atmospheric Science, Colorado State University, Fort Collins, Colorado 80523

[1] The adjective "daily" is used to denote both diurnal and semidiurnal variations.

vergence and vertical motion (Nitta and Esbensen 1974; McBride and Gray 1980), surface pressure (Haurwitz 1965; Haurwitz and Cowley 1973), cloudiness (Short and Wallace 1980; Minnis and Harrison 1984a,b,c; Warren et al. 1986; Susskind et al. 1987; Meisner and Arkin 1987), and outgoing longwave radiation (Duvel and Kandel 1985; Hartmann and Recker 1986; Slingo et al. 1987; Liebmann and Gruber 1988). In many cases these fluctuating fields can strongly interact with each other.

There have been very few published studies of GCM-simulated diurnal variability and most of these have focused on the tides. The earliest, by Hunt and Manabe (1968), is mainly of historical interest since the model used was far short of a comprehensive GCM; it omitted mountains, land–sea contrast, moisture, and diurnal forcing of the boundary temperature. In a more modern study, Zwiers and Hamilton (1968) studied the diurnal cycle simulated by the GCM of the Canadian Climate Center. They noted that, although the results showed many realistic features in the simulated semidiurnal and diurnal oscillations of surface pressure and winds, the simulated daily oscillations of precipitation were much weaker than observed. They suggested that this might be due to their model's use of prescribed cloudiness. Recently, tidal motions produced in assimilations with the forecast model of the European Centre for Medium Range Weather Forecasts have been described by Hsu and Hoskins (1989).

Tokioka and Yagai (1987) and Yagai (1989) used the 12-level GCM of the Japanese Meterological Research Institute (MRI) with a 1 mb top to investigate the tides produced in a January simulation. The MRI GCM is based on a predecessor to the GCM used in the present study, and has essentially the same latent heating parameterization. Fairly realistic external tidal modes are excited in the model, including various zonal wavenumbers and both diurnal and semidiurnal periods. These modes are strongly associated with diabatic heating in the lower troposphere, mainly following the geographical distribution of land and sea. Not surprisingly, a tropospheric version of the MRI model with its top near 50 mb produces much less satisfactory simulations of the tides (Yagai, personal communication 1989).

Although the primary forcing for the semidiurnal and diurnal atmospheric tides is warming due to solar absorption by ozone and water vapor (e.g., Chapman and Lindzen 1970), Lindzen (1978) suggested that theories of the semidiurnal tide could be brought into better agreement with observations by hypothesizing a semidiurnal forcing by latent heating with an amplitude of about 1 mm day^{-1} and a maximum near 0300 LST. Hamilton (1981b) provided support for this idea and suggested that the tidal response to tropospheric forcing largely follows the geographical details of the forcing, which are primarily due to land–sea contrast and the distribution of precipitation over the globe. He demonstrated that the semidiurnal tide shows strong seasonal and geographical variations, which appear to correlate with variations in the semidiurnal component of the latent heating, and interpreted these results as evidence that latent heating is an important forcing mechanism for both the semidiurnal and diurnal tides.

The GCM used in the current study is not suitable for simulation of the tides because its top is much too low (50 mb) and its vertical resolution is too coarse (about 2 km, on the average, through the troposphere). It can, nevertheless, be used to investigate consequences of the diurnal insolation cycle that are not significantly influenced by the tides. In particular, it can be used to investigate the diurnal variability of the hydrologic cycle. Although Malkus (1964) and Brier and Simpson (1969) suggested that daily variations in precipitation are forced by the tides, the idea has been met with skepticism (Lindzen 1978) on the grounds that the tidal moisture convergences are not strong enough to produce significant fluctuations of precipitation. At any rate, even if it were shown that tidal moisture flux convergences are in fact strong enough to balance diurnal or semidiurnal fluctuations in precipitation, it would not necessarily follow that the fluctuations of the precipitation rate are *caused by* the tides. Further discussion of cause and effect issues is given later.

The performance of a model can be evaluated by comparing its response to an imposed forcing with the observed response of the real-world system to the same forcing. The recent literature is replete with tests of GCMs based on evaluation of their response to seasonal forcing, interannual sea surface temperature anomalies due to El Niño and the like. Most of these tests require very long simulations because of the relatively long time scale of the forcing. Diurnal forcing can also be used to test models, and has the advantage that its time scale is relatively short, so that meaningful results can be obtained with a relatively brief simulation.

2. Experiment design

The diurnal variations of the hydrologic cycle simulated by the University of California at Los Angeles/Colorado State University (UCLA/CSU) GCM have been investigated. This model is essentially the same as the UCLA/GLA GCM, which has been described by Randall et al. (1989) and Harshvardhan et al. (1989). It is based on the UCLA GCM, which was developed at UCLA by A. Arakawa and collaborators. The UCLA/CSU GCM differs from the UCLA GCM primarily in that it has improved parameterizations of radiation (Harshvardhan et al. 1987) and cloud optical properties (Harshvardhan et al. 1989), and extensive new diagnostics, some of which are discussed in the following text.

In this paper, results are presented from a three-year simulation (currently being extended to five years).

The resolution used is 4° latitude by 5° longitude, with 9 levels extending from the surface to 50 mb. The time step used for the "dynamics" and the turbulent fluxes at the earth's surface is 450 s, and that for all other parameterized processes, including both terrestrial and solar radiation, is 1 h. The seasonally varying distribution of ground wetness is prescribed following Mintz and Serafini (1983). For the present study, results have been composited from the three Januarys and three Julys to make two datasets containing 90 days each.

In order to allow analysis of the simulated daily variability without archiving an excessive amount of data, daily values of the sine and cosine coefficients of the first two daily harmonics of selected fields were computed "on the fly" and saved on tape. Hereafter, these harmonics will be referred to as S_1 and S_2, respectively. The daily means of the same fields have also been saved, as well as the daily means of many additional fields. Finally, hourly results were collected for the entire run on a variety of fields at selected grid points and statistical significance was determined via chi-square tests (see the Appendix).

3. Simulated daily variations of the hydrologic cycle

In this section, global simulations of the seasonally varying diurnal and semidiurnal variations of the hydrologic cycle are presented, and compared with observations.

This study begins, however, by presenting the simulated and observed (Jaeger 1976) monthly mean precipitation distributions and their difference for January and July in Fig. 1. Note that the plots are logarithmically contoured. The model produces considerably more precipitation than observed, although the observed monthly means are very uncertain over most of the earth's surface. The geographical distribution of precipitation and its seasonal variations are quite realistic, however. For January, the storm tracks of the Northern Hemisphere winter are clearly depicted as are the precipitation maxima over tropical South America (considerably weaker in the model than in the observations) and southern Africa. The seasonal change of precipitation over Africa is fairly realistic. The precipitation minima associated with the subtropical highs are well represented in both seasons. For July, the model produces realistic precipitation maxima over eastern North America and Central Europe, although the latter is stronger than observed. The Indian summer monsoon is simulated, although it is weaker than observed, and does not penetrate far enough north. The GCM correctly produces a precipitation maximum near the tip of South America in both seasons.

Figure 2a shows maps of the simulated phase and amplitude of $S_1(P)$, the first diurnal harmonic of the precipitation rate P, for January and July. For both months, the amplitude reaches about 1.5 mm day^{-1} over the tropical oceans. Far from land, $S_1(P)$ tends to have a maximum near 0600 local time (LST). It is much stronger over the tropical continents, approaching 5 mm day^{-1} in the zonal mean for July and exceeding 6 mm day^{-1} for particular regions in July. For the most part, the maximum of $S_1(P)$ over the continents occurs in the afternoon, although for equatorial Africa in January the GCM produces a maximum of $S_1(P)$ near 0600 LST. Hamilton (1981a) found that for most of the stations for which he had data in the tropics the diurnal mode peaks near 1500 local time (LST), while a minority of points have maxima near 0600 LST. The latter are presumably oceanic points. (Of course, most of the data available to Hamilton was from continental stations, but he included island data whenever possible.) The July signal over the Northern Hemisphere continents, which has its maximum around 1400 LST, is much stronger than the January signal, which has its maximum around 0400 LST. For the Amazon region of South America, the January maximum of $S_1(P)$ is near 1200 LST in the northwestern part of the domain, and near 1800 LST in the southeastern part. A similar spatial variation can be seen in Fig. 4 of Meisner and Arkin (1987).

Figure 2b shows the corresponding results for $S_2(P)$. It is strongest over the tropical continents. Its zonally averaged amplitude reaches about 2.5 mm day^{-1} in the tropics, while over the tropical oceans it is slightly more than 0.5 mm day^{-1}. Its continental maxima tend to occur near 0300 LST (and 1500 LST), and its oceanic maxima tend to occur near 0600 LST (and 1800 LST). Hamilton (1981a) found that over the tropical continents the observed semidiurnal mode peaks at 0300–0400 LST (and 1500–1600 LST), about one hour later than simulated. For the tropical continents, the maximum amplitude of $S_2(P)$ in Hamilton's observations is about 1.35 mm day^{-1}; the model produces a much stronger signal, especially over tropical South America in January.

Hamilton concluded that oceanic precipitation has a strong semidiurnal mode but only a weak diurnal mode, while continental precipitation has both diurnal and semidiurnal variability. Model results in the current study are not consistent with this view. Figures 2 and 3 show that over the oceans the simulated diurnal mode is stronger in many places than the simulated semidiurnal mode.

These results show that the GCM produces a rather monotonous early afternoon precipitation maximum over warm continents. Although the observations do tend to show an afternoon maximum (e.g., Wallace 1975; Hamilton 1981a), the simulated maximum is generally earlier than observed and it is much too regular. In particular, the GCM does not reproduce the observed variations of the phase the precipitation over the North American continent in summer. As described by Wallace (1975), the observed precipitation

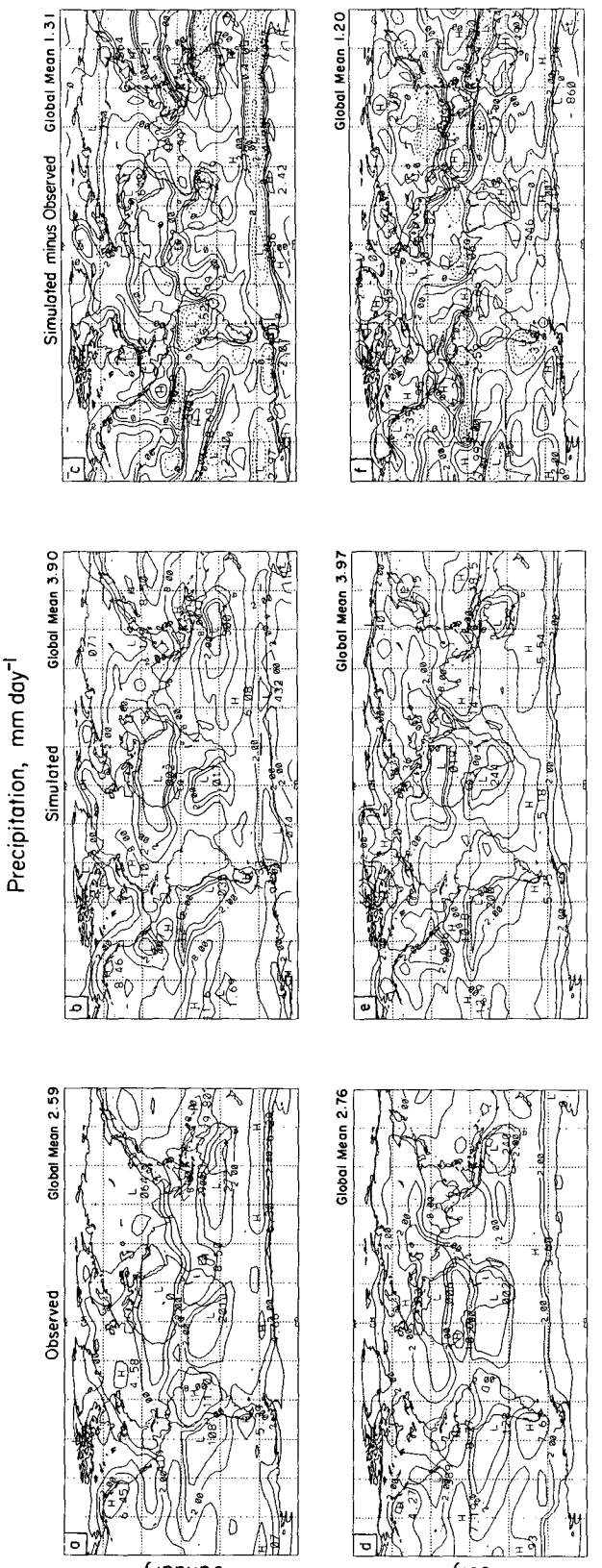

FIG. 1. The simulated and observed (Jaeger 1976) monthly mean precipitation distributions and their difference for January and July. All units are mm day^{-1}. For the simulated and observed means, the plotted contours are 1, 2, 4, 8, and 16 mm day^{-1}. For the difference maps, the plotted contours are -8, -4, -2 -1, 0, 1, 2, 4, and 8 mm day^{-1}. (a) January observed. (b) January simulated. (c) January difference between simulation and observation. (d) July observed. (e) July simulated. (f) July difference between simulation and observation.

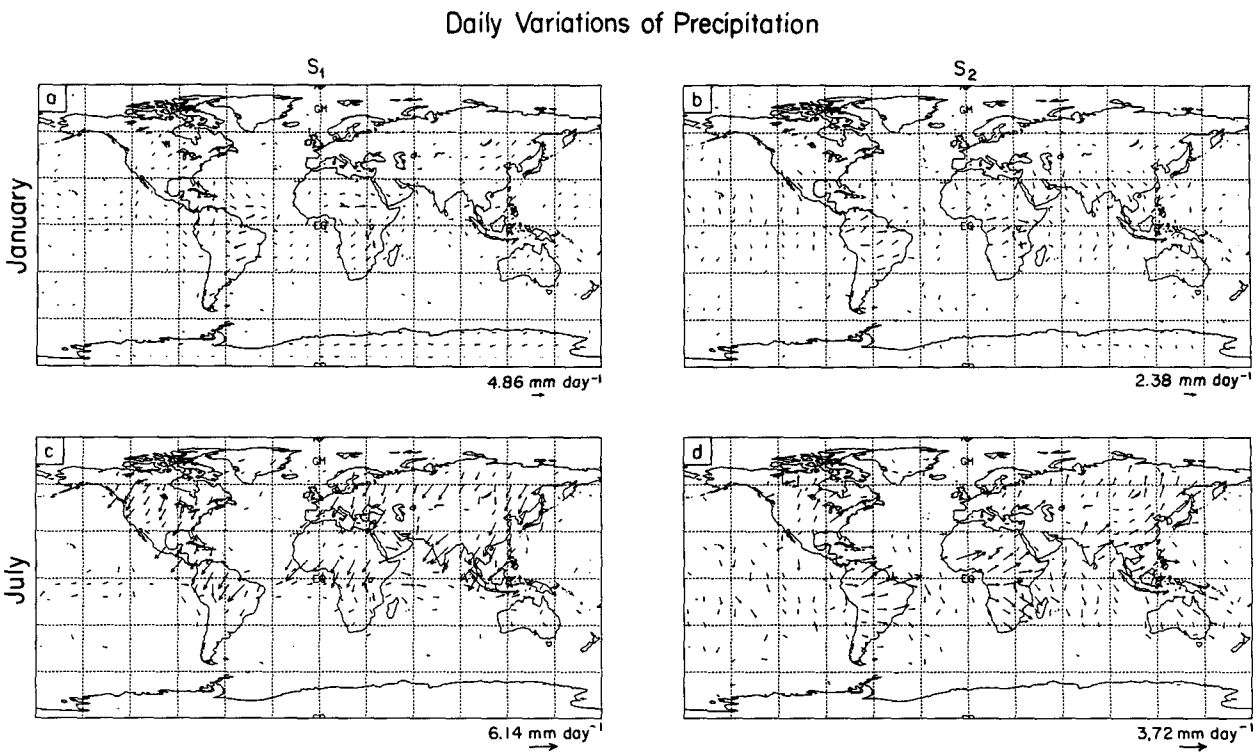

FIG. 2. The simulated phase and amplitude of $S_1(P)$ and $S_2(P)$, for January and July. The units are mm day^{-1}. Arrows are plotted only where the statistical significance parameter M exceeds 6; see Appendix for explanation. For $S_1(P)$, arrows pointing upward indicate maxima at local midnight, those pointing to the right indicate maxima at 0600 LST, etc. For $S_2(P)$, arrows pointing upward indicate maxima at local midnight, those pointing to the right indicate maxima at 0300 LST, etc. (a) $S_1(P)$ for January. (b) $S_2(P)$ for January. (c) $S_1(P)$ for July. (d) $S_2(P)$ for July.

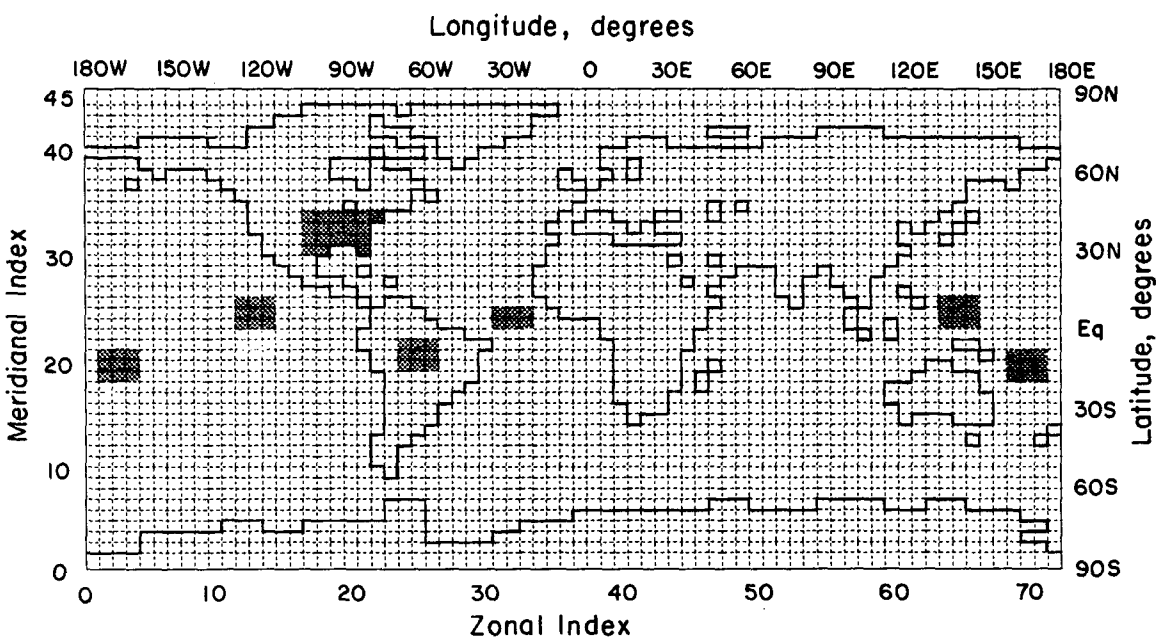

FIG. 3. The locations of the particular regions for which model results have been entered in Table 1.

maximum occurs in late afternoon, except in the upper midwestern United States where it occurs around midnight. These observed phase variations may be due in part to the influence of the nocturnal jet, which the present model cannot simulate because of inadequate vertical resolution (Randall et al. 1985). They may also be due in part to the eastward propagation of convective complexes generated over the Rocky Mountains during the afternoon. The present model cannot simulate such propagating mesoscale systems; presented with a situation in which they should occur, it will at best produce a daily-mean precipitation maximum in approximately the right place.

The simulated daily variability of the various components of the vertically integrated atmospheric moisture budget has been investigated. This budget is given by

$$\frac{\partial}{\partial t}\int_{p_T}^{p_s} q\,dp \Big/ g = -\nabla\cdot\left[\int_{p_T}^{p_s} (\mathbf{V}q)\,dp \Big/ g\right] + E - P, \quad (3.1)$$

where q is the specific humidity, p is the pressure, subscript S denotes the earth's surface, subscript T denotes the top of the model, g is the acceleration due to gravity, $\mathbf{V}$ is the horizontal velocity vector, E is the surface evaporation, and P is the precipitation. The first term on the right-hand side of (3.1) is the vertically integrated horizontal moisture flux convergence (MFC). The left-hand side is the time rate of change of the vertically integrated water vapor amount or precipitable water (PW). Hereafter, this is referred to as the storage term. The phase and amplitude of the first and second daily harmonics of the storage term was determined by analytically differentiating the corresponding harmonics of the PW itself. As is well known, for an average over more than a few days, the storage term of (3.1) is negligible. It can be significant, however, for daily variations.

The following results show that the diurnal and semidiurnal components of (3.1) are balanced in a variety of ways over the globe. It is tempting to interpret the balances in terms of cause and effect. For example, one way to think about (3.1) is that fluctuations of evaporation (driven by solar heating over land) and moisture flux convergence (driven by the large-scale motions over land or ocean) force fluctuations in precipitation and storage. From this point of view, the evaporation and the moisture flux convergence are the "forcing," while the precipitation and the storage are the "response." Of course, this is only a somewhat arbitrary interpretation, which may be valid in some cases but not in others. Another possibility is that fluctuations of precipitation are driven by processes not appearing explicitly in the moisture budget; for example, as discussed later there is some evidence that the fluctuations over the ocean are driven radiatively. In this case, one can view the precipitation as the forcing in (3.1). The response could appear, for example, as a drying (negative storage) when the precipitation rate is high and as a moistening (positive storage) when the precipitation rate is low. The point is that caution is needed in interpreting the various balances of (3.1) in terms of cause and effect.

Special attention is given to selected geographical regions (Fig. 3), which have been chosen because of their interesting characteristics, and the availability of observations: eastern North America (both January and July), the GATE region (July), the western equatorial Pacific Ocean (south of the equator for January, and north of the equator for July), tropical South America (January), the South Pacific Convergence Zone (January), and the ITCZ of the eastern north Pacific (July). Table 1 summarizes the results for these regions.

For eastern North America in January, the diurnal component of the storage roughly balances the evaporation while the diurnal component of the precipitation roughly balances the moisture flux convergence. The same pairings apply for the semidiurnal mode in January. The winter maxima of $S_1(P)$ and $S_2(P)$ tend to occur in the early morning in agreement with the observations of Hamilton (1981a). For July, on the other hand, the situation is more complicated. The diurnal and semidiurnal amplitudes of the evaporation are both quite strong with reinforcing maxima near noon. These are balanced by the remaining components of the moisture budget. In particular, $S_1(P)$ has an amplitude of 2.62 mm day^{-1} with a maximum near 1400 LST and $S_2(P)$ has an amplitude of 1.30 mm day^{-1} with maxima near 0130 and 1330 LST. The two modes together produce a strong afternoon precipitation maximum. The simulated seasonal changes in the phase of the precipitation maxima for North America are in qualitative agreement with the observations reported by Hamilton (1981a,b). Table 1 also shows that S_1(MFC) peaks shortly after 0200 LST. This is in qualitative agreement with the observations of Rasmusson (1967, 1968), who reported that over North America in summer the vertically integrated horizontal moisture flux and its divergence exhibit strong systematic differences between 0000 UTC and 1200 UTC; in the region east of the Rocky mountains, moisture converges at 1200 UTC (local morning) relative to 0000 UTC (local evening). Rasmusson concluded that the vapor flux oscillation over the continent is largely controlled by the low-level diurnal wind oscillation (Holton 1967; Bonner 1968), which primarily affects the lowest two kilometers of the atmosphere.

Observations (e.g., Jaeger 1976) show that tropical South America experiences a seasonal precipitation maximum in the northern winter, peaking January. The model simulates this broad seasonal maximum, although the simulated peak values occur in October.

TABLE 1. Summary of the simulated diurnal variation of the hydrologic cycle, for four selected regions and seasons. Each cell of the table gives the amplitude (mm day^{-1}) and phase (local time of maximum) for S_1 and S_2.

Location	Storage	Moisture flux convergence	Evaporation	Precipitation
Eastern North America, January	S_1: 1.14, 12.8 S_2: 1.09, 1.56	S_1: 1.63, 3.6 S_2: 0.65, 4.3	S_1: 1.61, 13.4 S_2: 0.92, 1.08	S_1: 1.14, 4.0 S_2: 0.43, 5.0
Eastern North America, July	S_1: 3.59, 10.8 S_2: 1.18, 11.0	S_1: 2.38, 2.2 S_2: 0.58, 6.8	S_1: 7.79, 12.8 S_2: 2.54, 0.4	S_1: 2.62, 14.1 S_2: 1.30, 1.5
Tropical South America, January	S_1: 3.12, 0.2 S_2: 4.21, 10.2	S_1: 12.7, 0.1 S_2: 2.45, 8.3	S_1: 9.61, 12.4 S_2: 4.06, 0.2	S_1: 1.06, 18.2 S_2: 1.77, 2.2
GATE region, July	S_1: 0.92, 6.0 S_2: 1.70, 9.1	S_1: 1.32, 4.6 S_2: 1.92, 9.3	S_1: 0.04, 10.1 S_2: 0.15, 5.3	S_1: 0.55, 2.5 S_2: 0.15, 9.4
Southern equatorial western Pacific, January	S_1: 2.61, 13.1 S_2: 0.80, 10.2	S_1: 3.05, 13.5 S_2: 0.55, 9.2	S_1: 0.22, 0.3 S_2: 0.12, 5.5	S_1: 0.38, 16.9 S_2: 0.54, 5.5
Northern equatorial western Pacific, July	S_1: 1.03, 18.0 S_2: 0.74, 9.8	S_1: 0.94, 18.0 S_2: 0.76, 9.8	S_1: 0.08, 21.6 S_2: 0.74, 8.8	S_1: 0.07, 2.3 S_2: 0.38, 5.4
South Pacific convergence zone, January	S_1: 0.84, 15.7 S_2: 0.70, 8.1	S_1: 0.85, 16.5 S_2: 0.98, 7.5	S_1: 0.05, 18.8 S_2: 0.20, 6.0	S_1: 0.21, 21.2 S_2: 0.57, 6.2
ITCZ of the eastern north Pacific, July	S_1: 0.83, 14.1 S_2: 2.46, 10.2	S_1: 0.38, 16.1 S_2: 0.15, 5.2	S_1: 0.05, 4.4 S_2: 0.15, 5.2	S_1: 0.57. 0.9 S_2: 0.43, 5.7

For the Amazon basin in January, the GCM produces a strong $S_1(P)$ signal with a maximum near 1800 LST, and an even stronger $S_2(P)$ signal with maxima near 0200 and 1400 LST. Table 1 shows, however, that most of the action in the diurnal component of the simulated hydrologic cycle consists of nearly compensating signals in evaporation and MFC; in other words, the simulated diurnal cycle of evaporation is roughly balanced by moisture flux *divergence*.

The observed diurnal variations of the GATE region are not very well simulated by the model. The observations show an afternoon precipitation maximum in August (e.g., Gray and Jacobsen 1977), while the model results for July, given in Fig. 2 and Table 1, show a rather chaotic pattern with no strong signal. (Note that the arrow length scale differs from panel to panel in Fig. 2 and in similar figures to follow.) The observed afternoon precipitation maximum in the GATE region may be due to westward propagating squall disturbances that form over the African continent (Gray and Jacobsen 1977); as already mentioned, the GCM is not capable of simulating such propagating mesoscale systems.

Elsewhere over the tropical oceans, the model fares somewhat better. Gray and Jacobson (1977) found a tendency for a morning precipitation maximum in the tropical western Pacific. They suggested that the morning precipitation is characteristic of oceanic regions far from land. Their observations for the Pacific region were supported by the study of Murakami (1983), who used GMS-1 infrared data to analyze the diurnal variation of deep convection over Southeast Asia and the adjacent oceanic regions. The tendency for a simulated maximum of $S_1(P)$ near 0600 LST for the western Pacific is evident in Fig. 2. According to Table 1, for the north equatorial western Pacific in July there are simulated weak morning maxima for both $S_1(P)$ and $S_2(P)$. For S_1, the principal balance is between MFC and storage. For the south equatorial western Pacific in January, the model produces maxima of $S_2(P)$ at 0600 LST and 1800 LST and a weaker afternoon maximum in $S_1(P)$. Both Gray and Jacobson and Murakami reported that the observed diurnal cycle of precipitation over the oceans is strongest where the mean convective activity was most intense. This is also consistent with the results, as can be seen by comparison of Fig. 1 with Fig. 2.

For the South Pacific Convergence Zone (SPCZ) in January, the GCM produces a moderate signal in $S_2(P)$ with maxima near 0600 LST (and 1800 LST). In this case, storage and precipitation both oppose the MFC; this is consistent with (but does not prove) the hypothesis that the fluctuations of the MFC are forcing the fluctuations of precipitation. The signal in $S_1(P)$ for the SPCZ in January tends to peak at about 2100 LST. The superposition of $S_1(P)$ and $S_2(P)$ produces an evening maximum of precipitation in the SPCZ, in agreement with the observations of Albright et al. (1985) and Meisner and Arkin (1987).

Finally, for the ITCZ of the eastern north Pacific Ocean in July, the GCM produces moderately strong signals in both $S_1(P)$ and $S_2(P)$, with maxima near 0100 LST and 0600 LST (and 1800 LST), respectively. For this region, both precipitation and MFC oppose storage. It is clear from the phase relationships that in this case the daily fluctuations of precipitation are not *forced by* the MFC, even though vigorous daily fluctuations of the MFC are present.

Figure 4 shows maps of the simulated phases and amplitudes of S_1(storage) and S_2(storage). Comparison with Fig. 2 shows a strong correlation between the *amplitudes* of the storage term and those of the precipitation rate. For July, the diurnal mode of the storage term has a maximum in the late morning over eastern North America and an early evening maximum over the western part of the continent. For equatorial South America in January, the maximum of S_1 occurs at about 0300 LST. The daily fluctuations of the storage term presented in Fig. 4 imply daily fluctuations of PW that are typically only a few percent of its total, and well within the uncertainty of the observations.

Figure 5 shows maps of the corresponding results for the MFC. The amplitude of S_1(MFC) exceeds 10 mm day^{-1} over the tropical land masses, and greatly exceeds the amplitude of $S_1(P)$. In fact, S_1(MFC) is large even in some places that are not particularly rainy. For example, there is substantial daily variation of the moisture convergence in the desert regions of southwestern North America and also in the Sahara.

Hastenrath (1967) found systematic 0000–1200 UTC differences of the horizontal moisture flux in the Caribbean and the Gulf of Mexico. He speculated that land–sea contrasts play a role in the forcing. Hastenrath's observations were supported by a study of Nitta and Esbensen (1974), who used BOMEX data to detect a 0000–1200 UTC oscillation of the horizontal mass divergence in the western Atlantic trades with an amplitude of 3×10^{-6} s^{-1} near the 700-mb level. Nitta and Esbensen also found diurnal oscillations of the vorticity and temperature, and diurnal wind fluctuations with an amplitude of about 1.5 m s^{-1}. They pointed out that BOMEX radar echoes analyzed by Hudlow (1970) show an early morning maximum in cumulus activity and suggested that this might be related to the diurnal oscillations of the large-scale motion field. For January, the GCM results show a morning maximum of the MFC in the western Atlantic trades. No clear signal appears in the July results.

Finally, Fig. 6 shows the simulated daily variations of the evaporation. Not surprisingly, the signal is very strong over the tropical and summer hemisphere continents, but it negligible over the oceans. Both $S_1(E)$ and $S_2(E)$ have maxima slightly after noon. Comparison with Figs. 5 and 6 shows that over land the daily variations of the evaporation are mainly balanced by those of the MFC.

Next the cloudiness fluctuations associated with the daily variations of precipitation are investigated. For brevity, the discussion is limited to upper tropospheric clouds. Figure 7 shows maps of the simulated phases and amplitudes of the first and second daily harmonics of the simulated upper tropospheric (pressure less than 400 mb) cloudiness. The amplitudes are largest in the tropics, particularly over land. Most of the action is in S_1. For tropical South America in January, the maxima occur between 1800 LST and midnight. In contrast,

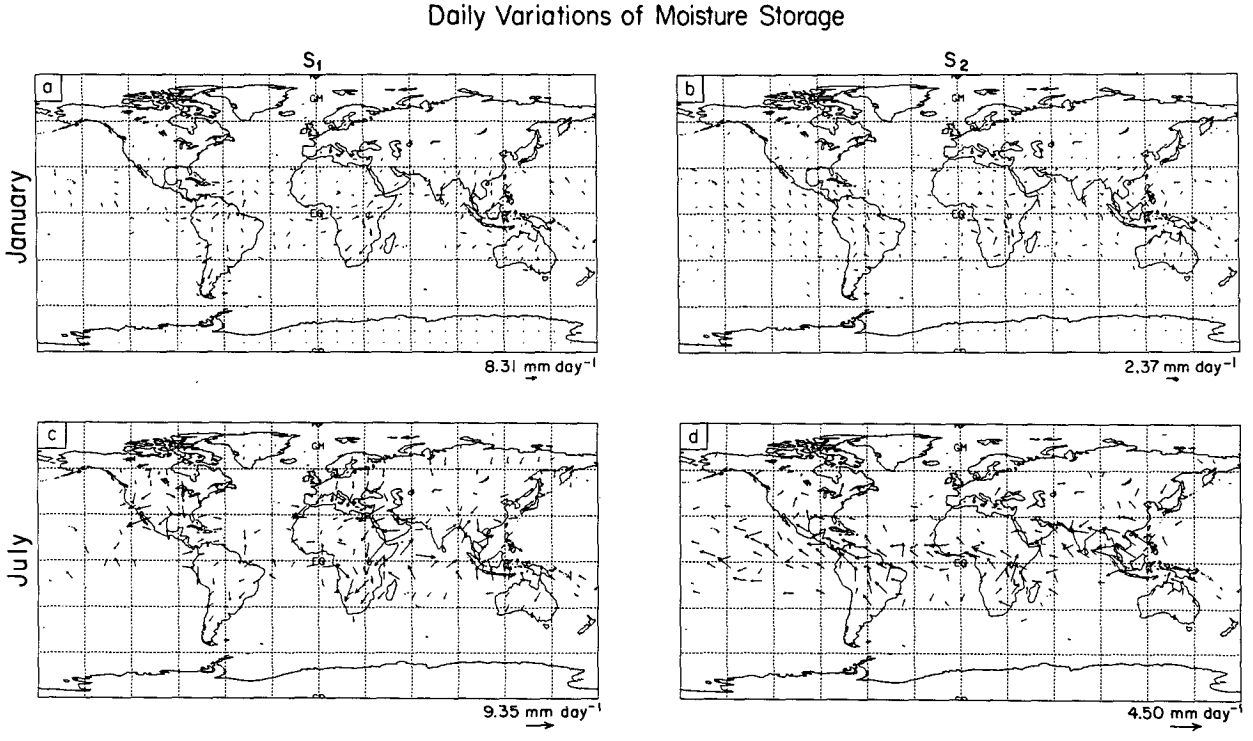

FIG. 4. As in Fig. 2, but for the storage term (3.1).

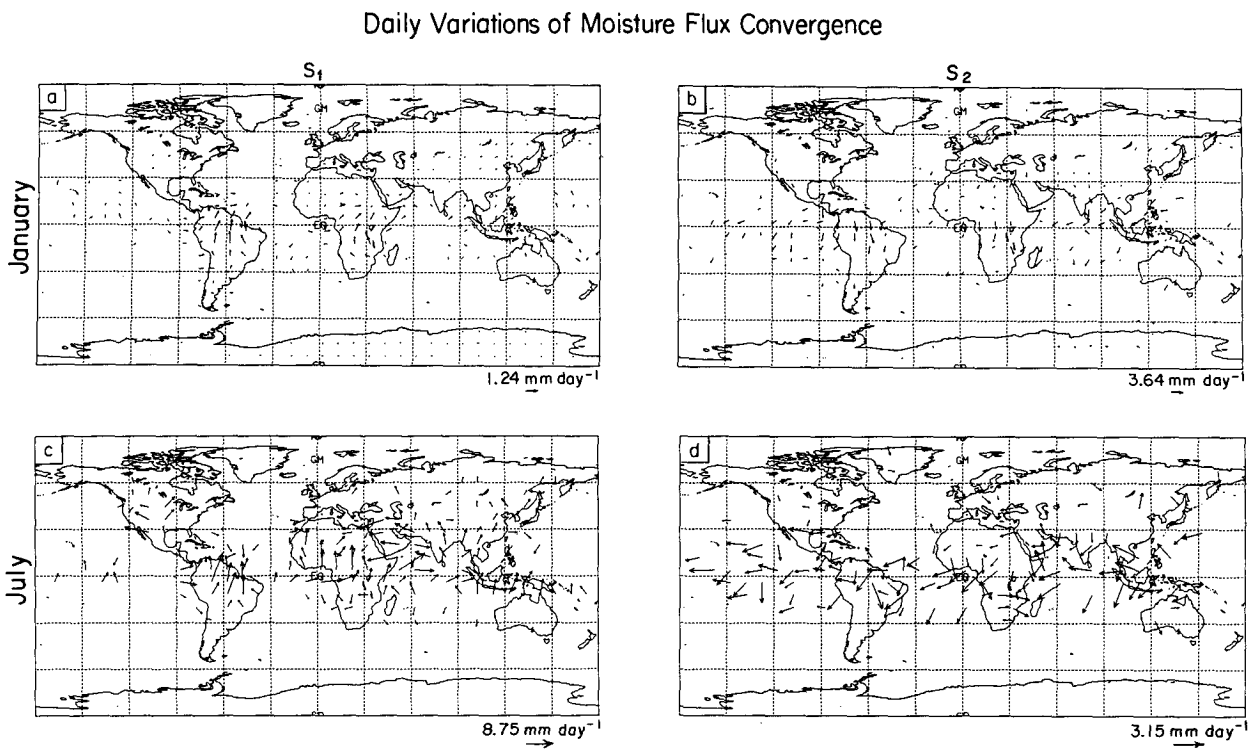

FIG. 5. As in Fig. 2, but for the convergence term of (3.1).

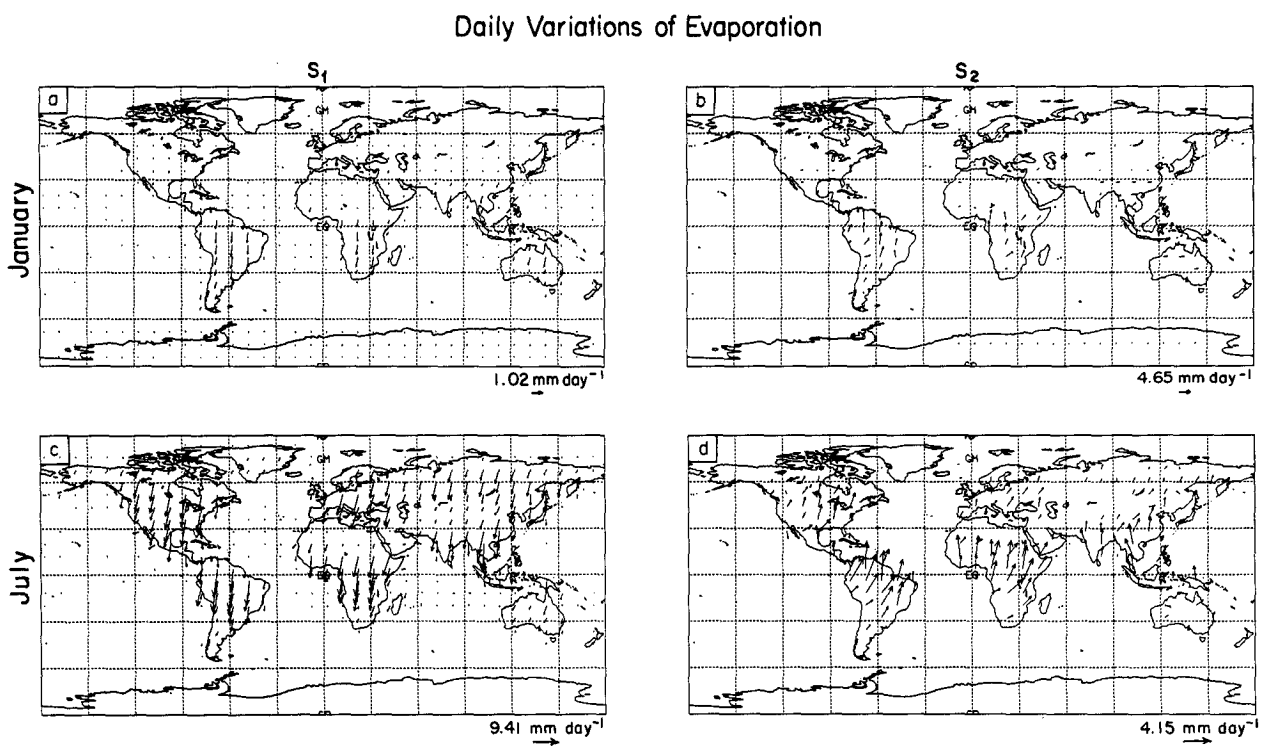

FIG. 6. As in Fig. 2, but for the evaporation term of (3.1).

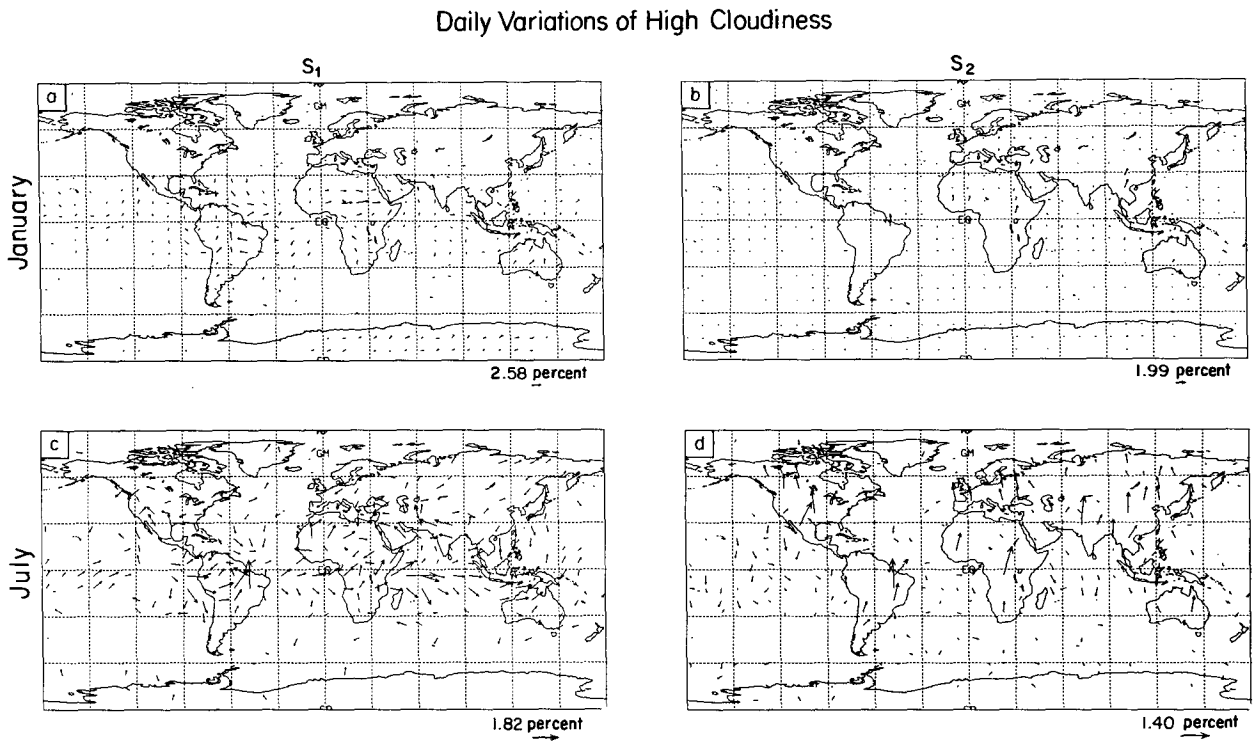

FIG. 7. As in Fig. 2, but for the upper tropospheric (pressure less than 400 mb) cloudiness.

for tropical North Africa in January the maxima occur near 0600 LST. Over the open oceans the maxima tend to occur between midnight and 0600 LST. This is in broad agreement with the observations of Murakami (1983). Exceptions are the South Atlantic and the SPCZ, both in January, where simulated maxima tend to occur in the late afternoon in agreement with the observations of Meisner and Arkin (1987). Note that the simulated precipitation maxima in these regions also tend to be in the late afternoon (Fig. 2).

Keenan et al. (1989) have recently published observed diurnal variations of high cloudiness over northern Australia and neighboring ocean regions within a few hundred kilometers of the coast for the southern summer. They found a maximum of high cloudiness near 1800 LST over land and near noon over the neighboring ocean. The current GCM results are not consistent with these observations; the GCM produces a high cloudiness maximum near 0200 LST for northern Australia in January.

Figure 8 shows maps of the phase and amplitude of the first and second daily harmonics of the simulated vertically integrated atmospheric cloud radiative forcing (ACRF), which is the difference between the actual radiative heating of the atmosphere and that which would occur in the absence of clouds (e.g., Harshvardhan et al. 1989, Randall et al 1989). The diurnal insolation cycle naturally tends to produce a maximum near 1200 LST, and just such a maximum is apparent at most points for both S_1(ACRF) and S_2(ACRF). Exceptions occur when the diurnal cycle of the ACRF is significantly influenced by the diurnal cycle of the cloudiness itself. For example, the maximum of the ACFR occurs near 0900 LST in the equatorial western Pacific where the diurnal cycle of high cloudiness produces a strong diurnal signal in the infrared warming of the atmospheric column.

In an analysis of the GATE data, Foltz and Gray (1979) showed that there is a diurnal variation of middle-tropospheric temperature with an amplitude of about 0.5°K and a maximum at about 1400 LST. Figure 9a shows the simulated variation with local time of the vertically varying temperature at the GATE point in our model for July conditions. The phase and amplitude are in reasonable agreement with the observations. Figure 9b shows the corresponding model results for the Marshall Islands region. A similar but somewhat stronger signal is evident. The figures suggest that the semidiurnal component of the temperature fluctuations is stronger at the lower levels. No attempt has been made to analyze this.

The model results show a wide variety of diurnal and semidiurnal fluctuations of the various components of the hydrologic cycle even if land or only ocean points are considered. Only weak general statements can be made. Taken together, these results suggest that the tropical ocean points in the model tend to experience nocturnal or early morning precipitation max-

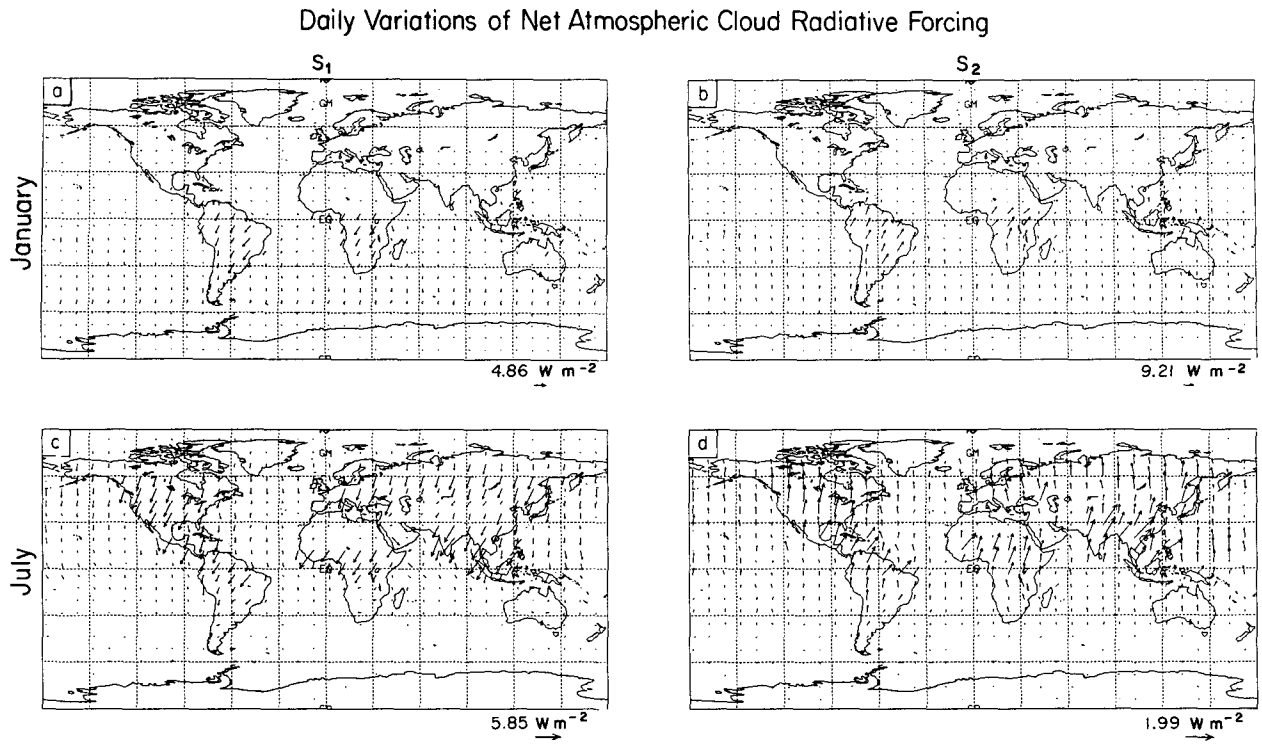

FIG. 8. As in Fig. 2, but for the vertically integrated atmospheric cloud radiative forcing.

ima, while the land points in the tropics and the summer hemisphere tend to experience afternoon or evening precipitation maxima.

4. Why is there a diurnal cycle of precipitation over the oceans?

a. Background

Three mechanisms that have been suggested for producing daily oscillations of precipitation over the oceans are considered:

1) *Direct radiation–convection interactions.* According to this simple hypothesis, atmospheric solar absorption during the day is concentrated in the upper portion of cloud masses associated with convection. This upper-level heating represents a stabilizing influence because it tends to decrease the lapse rate of temperature. At night, the destabilizing effects of longwave cooling dominate. This suggests that radiative forcing tends to favor more intense precipitation at night, provided that there is some background process to force a time-mean precipitation. This hypothesis does not require diurnally varying large-scale motions, although it certainly does not preclude their existence, and might account for them as a forced response to the combined effects of the radiative and latent heating.

2) *Radiation–dynamics–convection interactions.* This is the idea advocated by Gray and Jacobson (1977), Foltz and Gray (1979), McBride and Gray (1980), and Ackerman and Cox (1981). Day–night differences in atmospheric radiative heating have one vertical profile in the cloudy, convectively active region, and a different profile in neighboring clear regions. As a result, the cloudy region experiences cooling relative to its clear surroundings during the day, and warming at night. These radiative effects induce day–night differences in vertical motions; in particular, upper tropospheric rising motion is enhanced in the cloudy region during the night, and suppressed in the cloudy region during the day. The result is an early morning precipitation maximum. McBride and Gray (1980) presented observational evidence that the large-scale vertical motion does indeed undergo systematic day–night changes in convective weather systems over the tropical oceans. They found that the mean upward vertical velocity in the disturbed marine atmosphere tends to be larger in the morning than in the evening. This somewhat complex mechanism involves both cloud–radiation interactions and spatially varying cloudiness, as well as diurnally varying large-scale vertical motions.

3) *Remote influence of the continents.* According to this hypothesis (Silva Dias et al. 1987), day–night differences in atmospheric heating over the continents drive large-scale motion systems that extend over (or propagate to) the neighboring oceans. These motions exhibit systematic daily variations associated with the

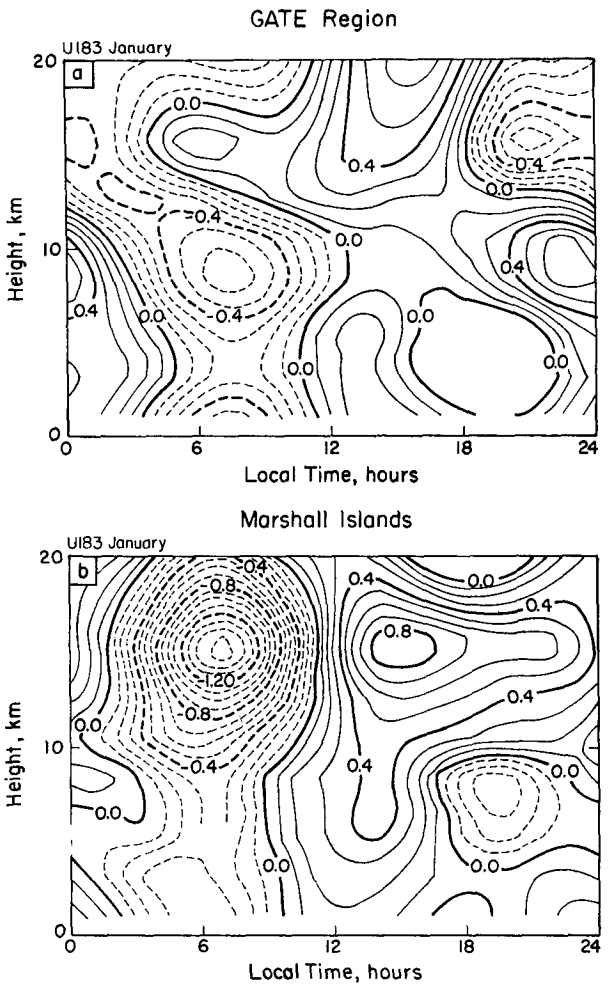

FIG. 9. (a) The simulated variation with local time of the vertically varying temperature at the GATE point in our model, for July conditions. (b) The corresponding model results for the Marshall Islands region.

diurnally varying continental heating that forces them. In this way, daily oscillations of precipitation over the oceans are excited. Since this hypothesis requires land–sea contrasts, it could not operate on an ocean-covered planet.

These three ideas are not mutually exclusive; each can be partly right. It is reasonable to use the UCLA/CSU GCM to test them, since as previously discussed in section 2, the model produces somewhat realistic daily variations of the oceanic precipitation.

In addition to the three previously mentioned mechanisms for producing a diurnal cycle of precipitation over the oceans, the possible role of a diurnal cycle of the sea surface temperature should also be considered. Under clear skies and light wind conditions, there is a slow rise in temperature to a late afternoon maximum followed by a rapid drop at night. The amplitude ranges from a few tenths of a degree to on the order of one degree, depending on conditions. The diurnal cycle of the sea surface temperature has been measured and modeled by many investigators (e.g., Ostapoff and Worthem 1974; Greenhut 1978; Price and Weller 1986) who have discussed its implications for convective activity and precipitation. Of course, this mechanism cannot be simulated by the current atmospheric GCM, in which the sea surface temperatures are externally prescribed.

b. Diurnal variations of precipitation on Seaworld

To investigate the role of land–sea contrast in forcing the observed daily variability of precipitation over the oceans, the results have been studied of the two "Seaworld" simulations reported by Randall et al. (1989). The first run included all of the model's physical parameterizations, while the second omitted the effects of clouds in both the solar and terrestrial radiation parameterizations. The sea surface temperatures of Seaworld are prescribed and zonally uniform and correspond to perpetual "July" conditions. Perpetual July earth–sun geometry was also prescribed. The key simplifications of Seaworld are the fixed boundary temperature with no land points, the lack of mountains, and the zonal uniformity of the boundary conditions. The results presented by Randall et al. (1989) were based on the last 60 days of two 90-day runs. For the present study, each simulation has been extended to 120 days, and the last 90 days of each have been analyzed.

The radically different mean states obtained in the two runs have been discussed by Randall et al. (1989); only a brief summary is given here. The cloudy run is the warmer and more humid of the two. It has a single concentrated rainbelt in the Northern Hemisphere, while the cloud-free run has a broad precipitation maximum, with a belt of slightly enhanced precipitation in each hemisphere. In the cloudy run, the southern edge of the rainbelt is near the equator. The globally averaged precipitation is nearly the same in the two runs. Cumulus convection occurs much more frequently in the cloud-free run, but does not penetrate as deeply and does not precipitate as intensely. The Hadley Cell transports about twice as much mass in the cloudy run as in the cloud-free run. Correspondingly, the tropical easterlies and midlatitude westerlies are both enhanced in the cloudy run. Further details are given by Randall et al. (1989).

Figure 10 shows the simulated diurnal cycle of precipitation for the two runs, plotted as a function of latitude and local time, including only the contributions from S_1 and S_2. Both runs have morning maxima and afternoon minima; *these are an order of magnitude stronger in the cloudy run,* however, as would be predicted by Gray and his colleagues. The strongest features in the cloudy run occur near the equatorward

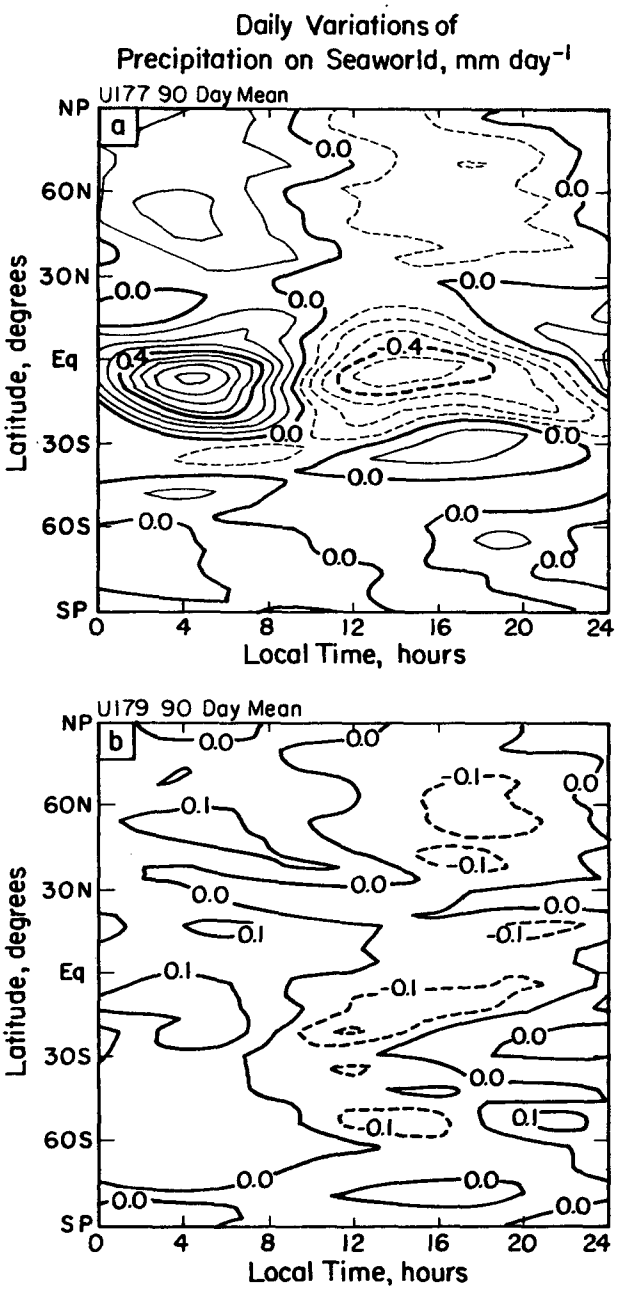

FIG. 10. The simulated precipitation for the (a) cloudy, and (b) cloud-free Seaworld simulations, plotted as a function of latitude and local time, including only the contributions from $S_1(P)$ and $S_2(P)$. The units are mm day^{-1}.

edge of the main rain band, close to the equator. The diurnal component is clearly much stronger than the semidiurnal component.

Figure 11 shows the diurnal variations of the time rate of change of the precipitable water, and Fig. 12 shows the corresponding results for the vertically integrated MFC. Both plots are in the same format as Fig. 10. The precipitation rate is positively correlated with MFC, as would be expected, although the two fields are far from identical. During the time when precipitation is most intense, the precipitable water content of the column is decreasing, although it decreases even more rapidly later in the day when the MFC attains its largest negative values.

Figure 13 shows the diurnal variations of the large-scale vertical motion at 200 mb. Again, the format of

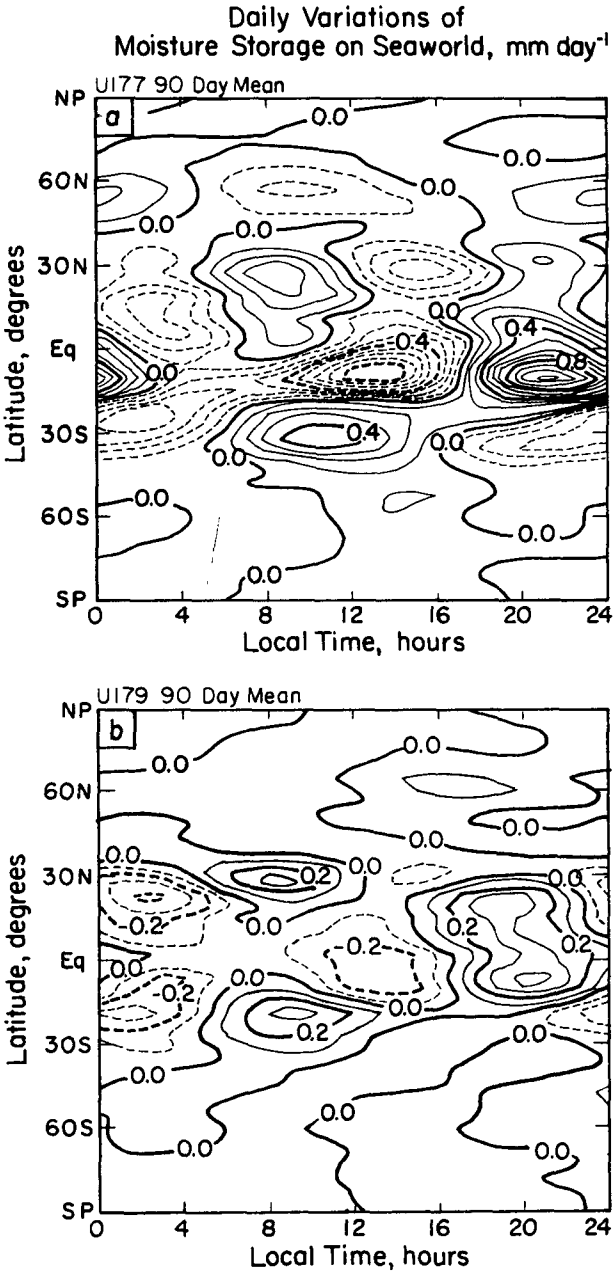

FIG. 11. As in Fig. 10, except for the diurnal variations of the time rate of change of the precipitable water.

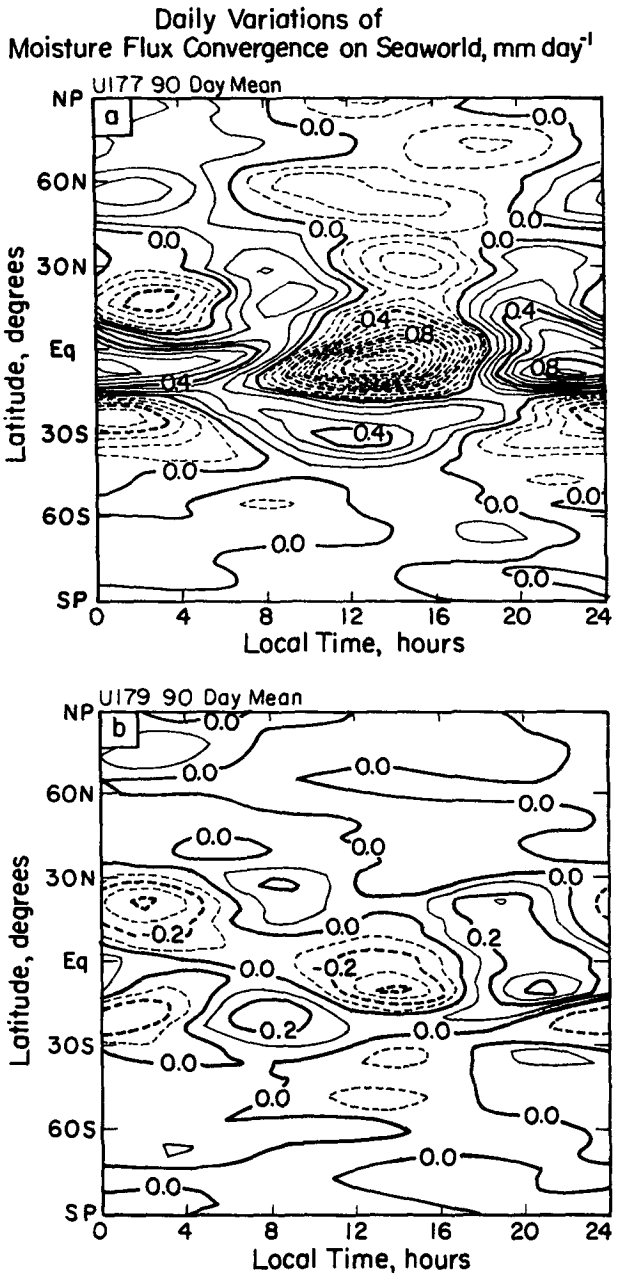

FIG. 12. As in Fig. 10, except for the corresponding results for the vertically integrated moisture flux convergence.

the plot is like that of Fig. 10. The vertical motion at 200 mb exhibits diurnal (S_1) variations, which are clearly correlated with precipitation events (cf., Fig. 10). The tropical signal is twice as strong in the cloudy run as in the cloud-free run. Large-scale rising motion at 200 mb slightly precedes the precipitation maximum, and large-scale sinking motion slightly precedes the precipitation minimum.

It is important to recognize that these correlations between the simulated daily variations of the large-scale vertical motion and the precipitation do not establish cause and effect; the precipitation signal could be forced by the vertical motion or vice versa. This is the familiar "chicken and egg" problem so often encountered in climate studies. The next subsection describes results from an even more highly idealized model that has been used to investigate this cause-and-effect issue.

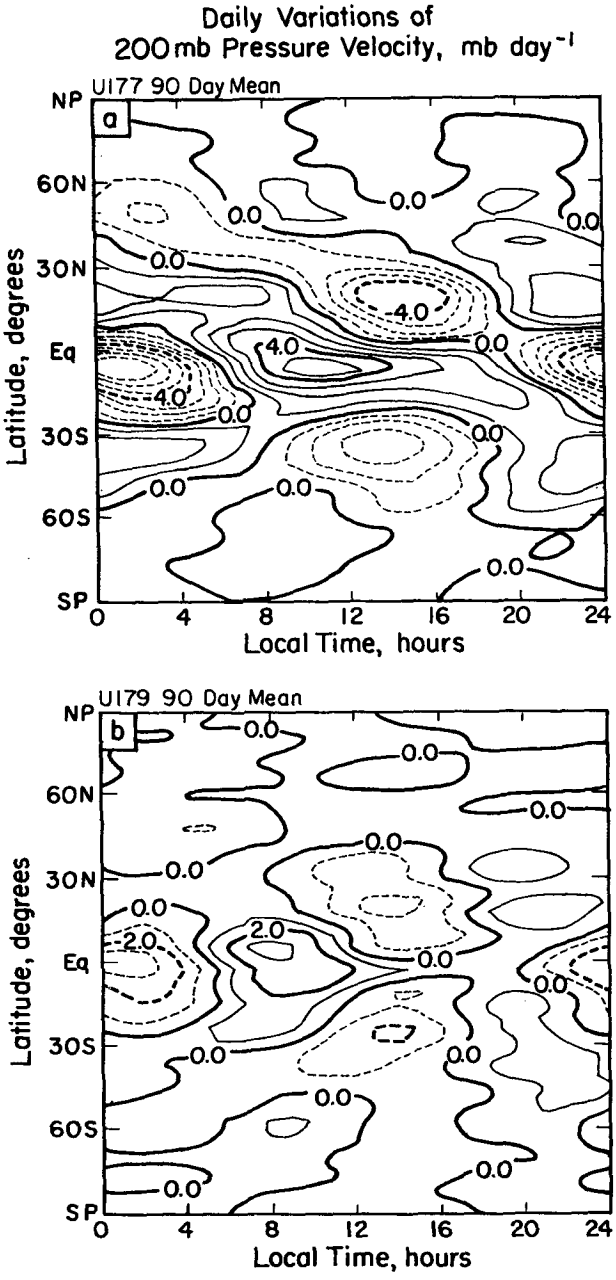

FIG. 13. As in Fig. 10, except for the diurnal variations of the large-scale vertical motion at 200 mb.

Also conducted was a third Seaworld experiment in which the diurnal insolation was replaced by an average, latitude-dependent, time-independent value for each longitude. The resulting large-scale circulation and hydrologic cycle were not significantly different from those obtained in the standard Seaworld simulation previously discussed.

c. *Experiments with a one-dimensional model*

In order to sort out the relative importance of diurnally varying radiative-convective interactions and diurnally varying large-scale vertical motion, a one-dimensional (1-D) model has been used, which represents a single vertical column in the GCM. The 1-D model includes all of the physical parameterizations of the GCM including cloud formation. It is not based on a copy of the GCM; instead, the 1-D model is the GCM itself, simply recompiled and with appropriate input data. Provisions have been made to include the effects of prescribed large-scale divergence, pressure gradient forces, and horizontal advection terms. This makes the 1-D model a very convenient testbed for new parameterizations that are intended for use in the global model. It can also be used to isolate particular physical processes as illustrated in the following text.

For all 1-D simulations discussed in this paper, nine levels were used, with a top at 50 mb, just as in the GCM simulations previously discussed.

In the first run, the 1-D model was forced with an idealized large-scale divergence field, based loosely on the composite GATE wave of Reed and his colleagues (Reed et al. 1977). The period of the wave was idealized to 97 hours (four days plus one hour). The model was initialized with a GATE sounding, and "spun up" for 100 simulated days. Then an additional 485 days (120 wave periods) were run, sampling the results once per hour. This procedure was designed to prevent any systematic diurnal bias in the input vertical motion field; each wave phase was sampled exactly five times at each of the 24 hours of the day.

Figure 14a shows the simulated precipitation, composited with respect to the phase of the wave. The model produces a systematic variation of precipitation over the wave with a maximum of about 25 mm day^{-1} when the upper-level wave divergence reaches a maximum at the 11 km level, and a minimum of about 5 mm day^{-1} when the upper-level divergence has a minimum. These results are reasonable in light of the GATE data as summarized by Reed et al. (1977).

As indicated in Fig. 14b, the diurnally forced 1-D model also produces a statistically significant diurnal cycle of the simulated precipitation with a maximum near 0600 LST, and an amplitude of about 1 mm day^{-1}. If the system were linear, large-scale dynamics could not be responsible for this signal, since the imposed large-scale divergence has no systematic variation

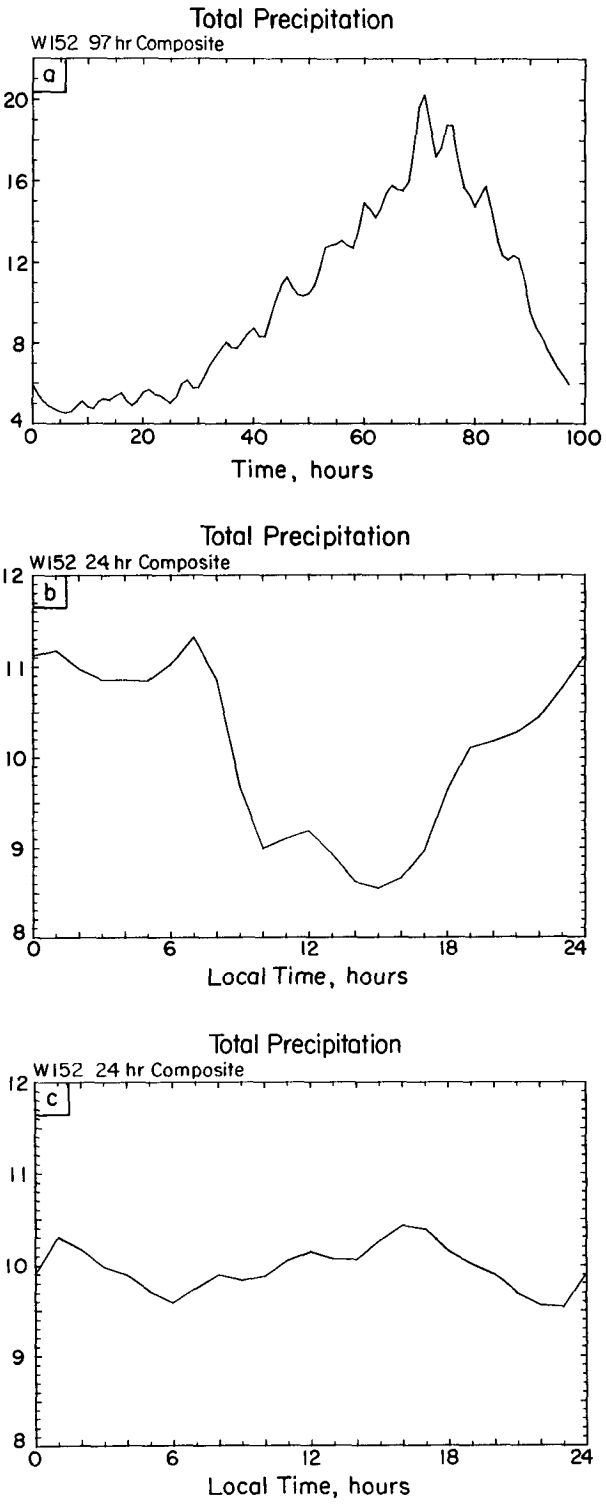

FIG. 14. (a) The simulated precipitation produced by the one-dimensional model composited with respect to the phase of the imposed "GATE wave." The units are mm day^{-1}. (b) The diurnal cycle of precipitation produced by the diurnally forced one-dimensional model. (c) As in (b), but for the one-dimensional model with daily-mean insolation. All units are mm day^{-1}.

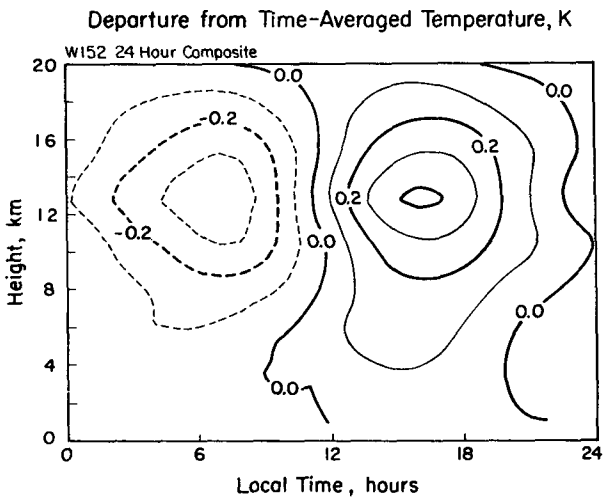

FIG. 15. The time–height variations of temperature produced by the diurnally forced 1-D model.

with time of day. Since the system is highly nonlinear, however, it is logically possible that the diurnal signal in the precipitation is indirectly produced by the GATE-wave forcing. To test this possibility, the run was repeated with time-averaged (nondiurnal) insolation. As shown in Fig. 14c, the amplitude of the diurnal signal of the precipitation was greatly reduced, and the weak remaining signal had a phase opposite to that obtained with diurnal forcing (and opposite to that observed). It is concluded that the diurnal cycle of precipitation in the diurnally forced run is produced by the diurnal cycle of the insolation, rather than by some nonlinear forcing originating in the prescribed vertical motion. The nondiurnal run produces essentially the same time-averaged and wave-composited precipitation as the diurnal run, however.

Figure 15 shows that the diurnally forced 1-D model produces an afternoon temperature maximum similar to that observed over the tropical oceans (see section 3). Figure 16 shows the time–height variations of the heating due to the following four processes: total latent heating (see Randall et al. 1989, for a discussion of this quantity), solar ACRF, terrestrial ACRF, and total ACRF. It is apparent that the solar ACRF produces a maximum heating a few hours in advance of the temperature maximum while at the same time the latent heating is actually decreasing. One concludes that the afternoon temperature maximum is due to solar warming.

These results demonstrate that direct radiative–convective interactions can produce daily variability of the precipitation and other variables with phase and amplitude similar to those observed over the tropical oceans, and also similar to those simulated in the Seaworld and earth simulations previously discussed.

d. Discussion

From the results presented in this section, it is possible to draw the following conclusions:

1) Even in the absence of land–sea contrasts, there would be a diurnal cycle of precipitation over the oceans with an amplitude near 1 mm day^{-1} in rainy regions, and a maximum near sunrise.

2) In the absence of radiatively active clouds the amplitude of this diurnal cycle would be much weaker.

3) Even in the absence of a systematic diurnal cycle in the large-scale vertical motion (and also without land–sea contrasts), there would still be a diurnal cycle of precipitation over the oceans with phase and amplitude qualitatively similar to those observed.

4) The stabilization due to absorption of solar radiation, primarily by clouds, tends to suppress convection during the afternoon, relative to the period before sunrise, to such an extent that *this mechanism alone can account qualitatively for the observed diurnal cycle of precipitation over the oceans.*

5) The observed diurnally varying large-scale vertical motions are not necessary to produce a qualitatively realistic diurnal cycle of precipitation over the oceans, and may be an effect of that cycle rather than a cause.

In summary, the observed and GCM-simulated diurnal cycles of precipitation over the oceans can be qualitatively accounted for by the direct suppression of daytime convection through solar warming of the atmosphere.

5. Earth simulations with no diurnal cycle

The diurnal cycle of precipitation is a linear oscillatory response to imposed oscillatory forcing. This is not the whole story, however. Evidence that nonlinear "rectifying" mechanisms produce a time-mean or net response of the hydrologic cycle to the oscillatory forcing was obtained by Randall et al. (1985; hereafter R85), who reported results from four July simulations performed with the UCLA GCM. In three of the simulations the diurnal cycle was included, while in the fourth it was omitted. Relative to the diurnal simulations, the nondiurnal simulation produced much more precipitation over land, and less over the oceans, although the globally averaged precipitation hardly changed. The nondiurnal run produced slightly less globally averaged cloudiness, but had a higher planetary albedo because in the diurnal runs there was more cloudiness at night than during the day. The results with the diurnal cycle were generally more realistic than those without the diurnal cycle.

A similar but more elaborate experiment was per-

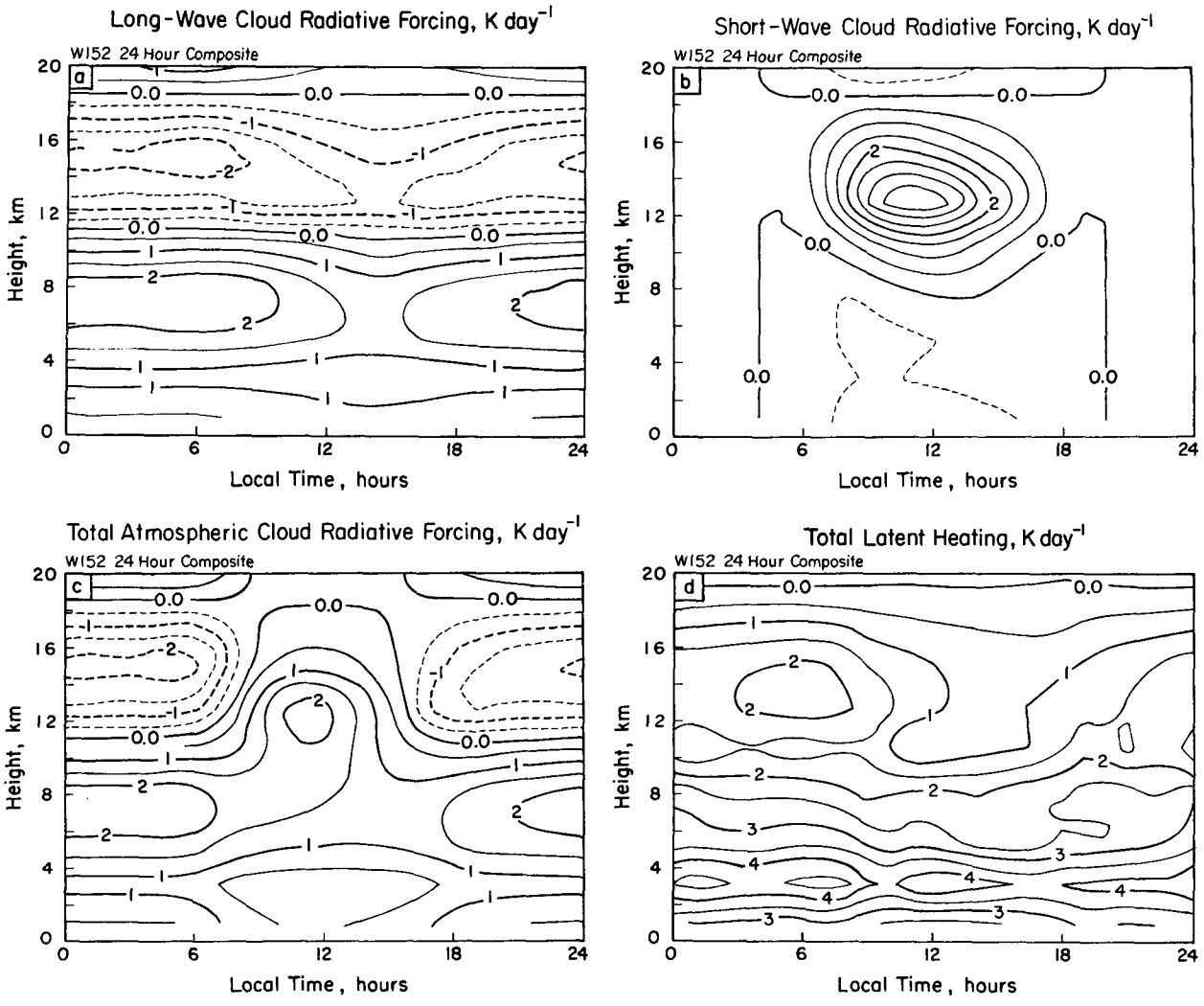

FIG. 16. For the diurnally forced 1-D model, the time–height variations of the heating due to the following four processes: (a) total latent heating; (b) solar ACRF; (c) terrestrial ACRF; and (d) total ACRF. All units are °K day^{-1}.

formed with the current UCLA/CSU GCM, which, it should be remembered, has been derived from the UCLA GCM used in the earlier study. The main change in the design of the new experiment is that the sample size has been increased by analyzing the July results from an ensemble of three nondiurnal June–July simulations, whereas R85 analyzed only a single nondiurnal July. As in the earlier experiment, the diurnal control results consist of three diurnal Julys taken from a multiyear simulation. Each of the three nondiurnal runs was initialized using 1 June conditions from one of the three Junes of the diurnal run, and was then "spun up" for 30 days before beginning of the July results that are discussed in the following text.

As mentioned earlier, the radiation parameterization was modified after the study of R85 was completed. The current UCLA/CSU model also uses a revised surface albedo prescription. In particular, the zenith-angle dependence of the surface albedo over both the oceans and the land surface has been included; the model used by R85 did not include this dependence. The current UCLA/CSU GCM also includes the effects of the water-vapor continuum, which makes humid boundary layers nearly opaque to infrared radiation. These various changes have influenced the following results.

All results presented here are based on sampling once per simulated hour. In both the diurnal and nondiurnal runs, all physical parameterizations including both solar and terrestrial radiation were evaluated once per simulated hour. In the nondiurnal run, the solar zenith angle was set to a longitude-independent value, chosen to give the correct daily mean insolation.

An examination is made of the response of the

earth's radiation budget to the diurnal cycle. First, the clear-sky components were considered. These are computed by "Method II" of Cess and Potter (1987). In this approach, the clear-sky values are sampled on each time step, regardless of whether or not cloud is present. [For a discussion of two alternative methods to define the clear-sky fluxes, see Cess and Potter (1987), Harshvardhan et al. (1989).] When the diurnal cycle is "turned on," the globally averaged clear-sky solar radiation absorbed by the earth increases slightly, by 1.42 W m^{-2}, i.e., the clear-sky albedo decreases. This can be attributed to zenith-angle effects, which cause the globally averaged ocean surface albedo to be about 0.75% smaller in the diurnal run. In the diurnal run, the zenith angle effects lead to large surface albedos near sunrise and sunset and low albedos at high sun angles. In the nondiurnal run the zenith angle is a constant at each latitude. The net effect is to decrease the clear-sky albedo in the diurnal run. This effect could be "tuned" out of the nondiurnal model by tinkering with the surface albedo prescription.

The clear-sky outgoing longwave radiation (OLR) decreases slightly in the diurnal run, by 1.76 W m^{-2}. The diurnally induced changes in the absorbed solar radiation and the OLR both tend to warm the earth; in combination, they amount to 3.18 W m^{-2}, which is comparable to the radiative forcing due to doubling CO_2.

From this point on, it is useful to consider the oceans and the land surface separately. Further results for the effects of the diurnal cycle on the earth's radiation budget are given in Table 2. The absorbed solar radiation (now including the effects of clouds) is larger in the diurnal results over both land and ocean, but particularly over the ocean. The globally averaged value increases by a substantial 4.85 W m^{-2}, which is about three times the increase due to clear-sky effects alone. This is consistent with the results of R85, who pointed out that the diurnal cycle reduces the planetary albedo because cloudiness occurs more often at night than during the day in the diurnal simulations.

When the effects of clouds are included, the OLR actually increases by a very modest 0.86 W m^{-2} in the diurnal run relative to the nondiurnal run. This is in contrast to the decrease in the clear-sky OLR previously mentioned. The increased OLR in the diurnal run must, therefore, be attributed to cloud effects; it is due to lower than average cloudiness during the day when the land surface temperatures are greatest.

TABLE 2. Summary of the *changes* in the components of the earth's radiation budget produced by turning on the diurnal cycle (i.e., values with the diurnal cycle, minus those without). All units are W m^{-2}.

Variable	Land means	Ocean means	Global means
Absorbed solar radiation	2.31	5.94	4.85
Outgoing longwave radiation	1.90	0.41	0.86
Net radiation into the earth–atmosphere system	0.40	5.54	3.99

The net radiation into the earth–atmosphere system increases by a very large 3.99 W m^{-2} in the diurnal run. Since the capacity of the atmosphere to store energy is quite small, most of the additional energy absorbed by the earth–atmosphere surface must be conveyed into the earth's surface one way or another. Accordingly, the globally averaged net surface energy flux increases in the diurnal run by 3.6 W m^{-2}. This consists of a 3.68 W m^{-2} increase over the oceans and a 3.39 W m^{-2} increase over the land surface.

Since an additional 3.39 W m^{-2} is being absorbed by the land surface, one might expect the land surface temperature to increase substantially in the diurnal run. Instead, just the opposite occurs. The globally averaged temperature of the land surface is actually 2.7°K cooler in the diurnal run; this is an enormous difference, considering that the sea surface temperatures on the neighboring oceans are exactly the same in both cases. The land surface temperature difference is most pronounced (almost 4.5°K) near 50°N, where the snow line occurs. The diurnal run has more snow on the ground because less snow has melted in the nondiurnal run; the rate of snow melt is less. The greater rate of snow melt in the nondiurnal run is apparently due to the perpetual solar illumination of the surface. The additional snow on the ground in the diurnal run leads to higher albedos and cooler temperatures over cold land areas such as extreme northern Asia. The additional energy input to the land surface in the diurnal run occurs mainly where the diurnal run has snow on the ground and the nondiurnal run does not. The energy is being used to melt the lingering snow.

Snow effects are not the primary mechanism for cooling the land surface; however, the cooler land surface temperatures of the diurnal run occur over almost all of the continental regions. For example, the average reduction in the tropical land surface temperature (between 30°S and 30°N) is about 2.7°K, the same as the globally averaged reduction.

What, then, is the primary mechanism responsible for the cooler land surface temperatures in the diurnal run? As the surface temperature increases in the course of a day, the surface sensible heat flux, the surface latent heat flux, and the surface infrared cooling rate all increase *nonlinearly* with the surface temperature.[2] An example will illustrate the relevance of this fact. In the

[2] For the surface sensible and latent heat fluxes this nonlinear increase results from the increase of the surface transfer coefficient with greater instability of the boundary layer. For the infrared cooling rate, it stems from the dependence of the upward surface longwave radiation on the fourth power of the ground temperature.

nondiurnal run, the land surface temperature does not vary much during a typical 24-h period. Suppose that, for a given 24-h interval of the diurnal run, the same *average* land surface temperature is maintained as in the nondiurnal run, but a sinusoidal variation of the temperature is forced by the diurnally varying insolation, such that for half of the day the temperature is warmer than the mean, and for the other half it is cooler than the mean. This scenario can be modeled crudely as follows: Let the land surface temperature obey

$$T = T_0 + A \sin(t), \tag{5.1}$$

where A is a positive amplitude, and t is a scaled time variable that runs from 0 to 2π during the course of a day. Let the increase of the net surface energy flux away from the surface with the surface temperature be governed by

$$H = H_0 + C\{\exp[B(T - T_0)] - 1\}, \tag{5.2}$$

where H_0 is the net-surface energy flux corresponding to $T = T_0$, and B is a positive constant. According to (5.2), when T increases beyond T_0, H *increases strongly;* and when T decreases below T_0, H *decreases weakly.* Substituting (5.1) into (5.2), it is found that

$$H - H_0 = C\{\exp[AB \sin(t)] - 1\}. \tag{5.3}$$

For concreteness, let $A = 20°\text{K}$, $B = 0.1°\text{K}^{-1}$, and $C = 10\ \text{W m}^{-2}$. Then, by integrating (5.3) numerically, we find that the average of $H - H_0$ over a day is about $80\ \text{W m}^{-2}$. This shows that, when H increases nonlinearly with T, a sinusoidal variation of T leads to an increase in the time-averaged net heat flux, all other things being constant.

Now turn the problem around. Let the time-averaged land surface temperature be T^*, different from T_0. When a sinusoidal temperature oscillation of amplitude A is imposed,

$$H - H_0 = C\{\exp[B(T^* - T_0) + AB \sin(t)] - 1\}. \tag{5.4}$$

Let the daily average value of H be H_0. Then (5.4) gives

$$\int_0^{2\pi} \{\exp[B(T^* - T_0) + AB \sin(t)] - 1\}\, dt = 0. \tag{5.5}$$

It follows that

$$T^* - T_0 = B^{-1} \ln \left\{ \frac{2\pi}{\int_0^{2\pi} \exp[AB \sin(t)]\, dt} \right\}. \tag{5.6}$$

By integrating (5.6) numerically, with the values of A and B given above, it is found that $T^* - T_0 = -2.5°\text{K}$. This admittedly contrived exercise illustrates that if the net energy flux away from the ground increases nonlinearly as the ground temperature increases, then a diurnal insolation cycle tends to reduce the time-averaged ground temperature, for a given time-averaged net surface energy flux.

The diurnally induced changes in the various components of the surface energy budget are rather complex; they are summarized in Table 3. The largest changes occur in the surface sensible heat flux, which increases, particularly in arid regions such as the Sahara and western North America, by an average of $3.98\ \text{W m}^{-2}$ (roughly 30% more than its value in the diurnal run); and in the net infrared cooling of the surface, which decreases by $3.89\ \text{W m}^{-2}$. The increased surface sensible heat flux in the diurnal run is due to the relatively warm maximum ground temperatures reached during the day, coupled with the strongly nonlinear increase of the surface transfer coefficient as the ground warms relative to the air. The reduced infrared cooling in the diurnal run is due to a reduction in the upward emission by the cooler land surface, by $16.1\ \text{W m}^{-2}$. The downward infrared radiation from the atmosphere to the land surface also decreases in the diurnal run, by $12.2\ \text{W m}^{-2}$. This is associated with the cooler surface air temperatures that accompany the cooler land surface temperatures. It is definitely *not* due to cloud effects; infrared cloud radiative forcing actually tends to warm the land more in the diurnal run.

In summary, the main effects of the diurnal cycle on the land surface energy budget are to increase the absorbed solar radiation over both land and ocean, but to decrease the daily mean surface temperature over land. Although the diurnal time-mean land surface temperature is cooler, its daily maximum values are, of course, much warmer. The cooling of the surface by the sensible heat flux increases, but that due to infrared radiation decreases.

TABLE 3. Summary of the *changes* in the components of the surface energy budget produced by turning on the diurnal cycle (i.e., values with the diurnal cycle, minus those without). All units are W m^{-2}. The net surface energy flux is defined positive downward. The sensible and latent heat fluxes are defined positive upward.

Variable	Land means	Ocean means	Global means
Net surface energy flux	3.39	3.68	3.60
Sensible heat flux	3.98	0.88	1.81
Latent heat flux	−0.79	2.81	1.73
Absorbed solar radiation	2.69	6.80	5.56
Upward infrared radiation	−16.10	−0.07	−4.69
Downward infrared radiation	−12.22	0.50	−3.32
Net upward infrared radiation	−3.89	−0.57	−1.58

The time-mean PBL depth over land diminishes sharply in response to the diurnal cycle because of the shallowness of the nocturnal PBL (see R85). In spite of this, the globally averaged precipitable water content hardly changes over land in the diurnal run. The diurnal cycle of the PBL depth effectively pumps moisture from the PBL into the free atmosphere (Mintz 1984); in the absence of a diurnal cycle, there is a tendency for moisture to be confined near the surface.

The results presented above suggest that a nondiurnal coupled ocean–atmosphere model may tend to produce unrealistically cool oceans and unrealistically warm continents. Some existing nondiurnal coupled ocean–atmosphere models do, in fact, tend to produce tropical oceans that are colder than observed (e.g., Washington and Meehl 1989; Miyakoda 1989), although, of course, there can by many possible explanations for this.

Table 4 shows the effects of the diurnal cycle on the globally averages precipitation rate and the globally averaged precipitable water. In the global mean, the diurnal cycle causes precipitation over land to decrease by 0.29 mm day^{-1} (about 8%), while over the oceans and globally it increases slightly. Precipitation over land decreases mainly in regions characterized by a "summer monsoon" regime in July. These include equatorial eastern South America, western equatorial Africa, eastern India, and Southeast Asia, as well as Central America. The diurnal cycle actually increases both the PBL moisture flux convergence and the surface evaporation in these regions, but this increased low-level moisture supply is not realized as precipitation. Instead, it is carried away by moisture flux divergence in the free atmosphere (Mintz 1984).

Because the monsoon regions experience both a decrease in precipitation and an increase in evaporation, they show up particularly well in maps of the difference in precipitation minus evaporation (as presented by R85). The implied diurnally forced change in the large-scale atmospheric moisture transport is out of the monsoon regions, and in fact away from the continents altogether, into precipitation centers over the oceans.

The results presented in Table 4 show that the globally averaged precipitable water is hardly affected by the diurnal cycle. Changes are at about the 1% level—too small to be meaningful.

TABLE 4. Summary of the *changes* in the precipitation and precipitable water produced by turning on the diurnal cycle (i.e., values with the diurnal cycle, minus those without).

Variable	Land means	Ocean means	Global means
Precipitation rate (mm day^{-1})	−0.29	0.21	0.07
Precipitable water (mm)	0.01	0.27	0.19

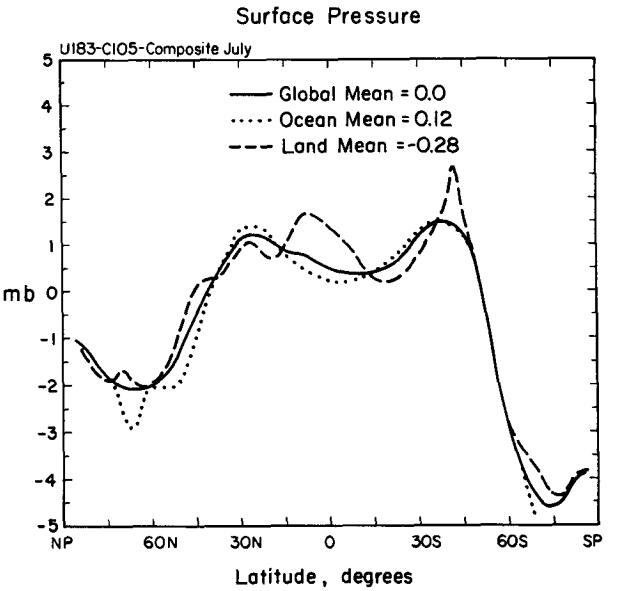

FIG. 17. The change in the distribution of the zonally averaged July mean surface pressure induced by the effects of the diurnal cycle.

Finally, as shown in Fig. 17, the diurnal cycle causes a remarkable shift of atmospheric mass from high latitudes into the tropics and subtropics, and an intensification of the "westerly" surface pressure gradients in the middle latitudes of both hemispheres, particularly near 55°S. The pressure difference between 45° and 70°S increases by about 6 mb.

These effects of diurnal forcing on the hydrologic cycle are generally similar to but weaker than those obtained by R85 with an earlier version of this same GCM. The somewhat weaker influence of the diurnal cycle in the newer model may be due to its incorporation of the effects of the water-vapor continuum, which blankets the surface, strongly limiting nocturnal cooling over land. It may also be partly accounted for by changes in the cloud optical properties and in the cloudiness distribution itself.

6. Summary and conclusions

The UCLA/CSU GCM has successfully simulated some aspects of the observed daily variability of the hydrologic cycle. This represents a useful test of the model's formulation and particularly its hydrologic cycle, since like all other GCMs it has been designed primarily to simulate the large-scale dynamics on time scales of several days or longer.

The model has been used to investigate the mechanisms that give rise to the observed diurnal and semidiurnal variations of precipitation over the oceans. The observed diurnal cycle can be qualitatively accounted for by direct radiation–convection interactions, al-

though indirect radiative–convective interactions mediated by the large-scale dynamics and the remote influence of the continents also play a part. Specifically, the absorption of solar radiation by clouds leads to a reduction of the precipitation rate in the afternoon (near the end of the daylight hours), relative to the early morning (near the end of the night). The observed diurnally varying large-scale vertical motion field is apparently *forced by* the diurnal cycles of radiative and latent heating; it is not a critical forcing agency for the observed diurnal cycle of precipitation over the oceans.

The GCM has also been used to study the effects of the diurnal cycle on the general circulation of the earth's atmosphere with particular emphasis on the hydrologic cycle and the surface energy budget. The results show that the diurnal cycle leads to a cooler land surface, with more evaporation and less sensible heat flux. The precipitation rate decreases over land in the diurnal run, particularly in the monsoon regions.

Obviously, the results depend on our model's formulation, and especially on its parameterizations of cloudiness and cumulus convection. To the extent that the model results agree with the observations, the parameterizations have passed a useful test. This study challenges other climate modelers to conduct similar analyses.

Finally, the version of the model used here cannot be used to simulate the atmospheric tides because its vertical resolution is too coarse and its top is too low. Results show that the simulated diurnal and semidiurnal components of the moisture flux convergence due the large-scale flow are quite significant; however, in comparison with the corresponding simulated (and observed) fluctuations of precipitation. There are, broadly speaking, two possibilities. One is that the tides do significantly influence the daily fluctuations of precipitation. There is some observational evidence for this (e.g., Rasmusson 1967, 1968; Nitta and Esbensen 1974). The second possibility is that the model is exaggerating the amplitudes of daily fluctuations of the moisture flux convergence, perhaps because of false resonances arising from the rigid-lid upper boundary condition. In either case, it would be useful to repeat the present analysis with the model top displaced to a higher level, as in the tidal simulations of Yagai (1989).

Acknowledgments. Dr. Thomas Bell of the Goddard Laboratory for Atmospheres provided helpful guidance on the statistical significance testing. Professor William Gray of Colorado State University contributed useful comments and suggestions as this research was being carried out. His interest is appreciated.

This research has been supported by NASA's Climate Program, through Grant NAG 5-1058 to Colorado State University. Computing resources were provided by the Numerical Aerodynamic Simulation Facility at NASA/Ames.

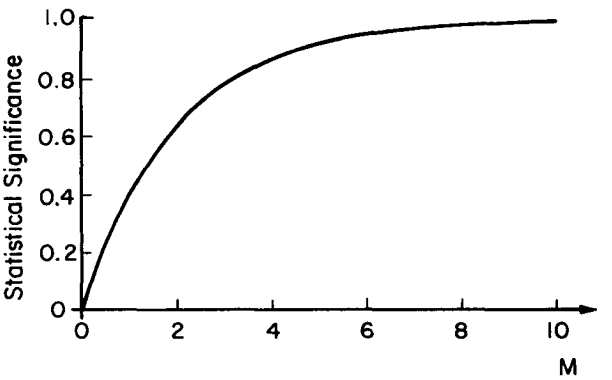

FIG. A1. The confidence with which the null hypothesis can be rejected, for a χ^2 distribution with two degrees of freedom, as a function of M [see (A.1)].

APPENDIX

Statistical Significance Tests

To investigate the statistical significance of the results, a chi-squared test with two degrees of freedom has been used. Let A and B be the sine and cosine coefficients of the first or second harmonic of some analyzed field. Let an overbar denote an average, and let $\sigma^2(\ )$ denote a standard deviation. Then it is required that

$$\frac{2N[(\bar{A})^2 + (\bar{B})^2]}{[\sigma^2(A) + \sigma^2(B)]} > M, \qquad \text{(A.1)}$$

where N is the number of independent samples, and M is chosen to reject the null hypothesis with the desired level of confidence. As shown in Fig. A1, $M = 9.2$ for 99% confidence. For given values of the means and standard deviations, (A.1) shows that the statistical significance increases linearly with the sample size.

It has been assumed that the diurnal and semidiurnal modes on successive days are independent. This assumption cannot be justified with any rigor.

REFERENCES

Ackerman, S. A., and S. K. Cox, 1981: GATE Phase III mean synoptic-scale radiative convergence profiles. *Mon. Wea. Rev.*, **109**, 371–383.

Albright, M. D., E. E. Recker, R. J. Reed and R. Dang, 1985: The diurnal variation of deep convection and inferred precipitation in the central tropical Pacific during January–February 1979. *Mon. Wea. Rev.*, **113**, 1663–1680.

Benton, G. S., and M. S. Estoque, 1954: Water vapor transfer over the North American continent. *J. Meteor.*, **11**, 462–477.

Bonner, W. D., 1968: Climatology of the low-level jet. *Mon. Wea. Rev.*, **96**, 833–850.

Brier, G. W., and J. S. Simpson, 1969: Tropical cloudiness and precipitation related to pressure and tidal variations. *Quart. J. Roy. Meteor. Soc.*, **95**, 120–147.

Cess, R. D., and G. L. Potter, 1987: Exploratory studies of cloud radiative forcing with a general circulation model. *Tellus,* **39A,** 460–473.

Chapman, S., and R. S. Lindzen, 1970: *Atmospheric Tides.* Dordrecht, 200 pp.

Duvel, J. P., and R. S. Kandel, 1985: Regional-scale diurnal variations of outgoing infrared radiation observed by METEOSAT. *J. Climate Appl. Meteor.,* **24,** 335–349.

Foltz, G. S., and W. M. Gray, 1979: Diurnal variation in the troposphere's energy balance. *J. Atmos. Sci.,* **36,** 1450–1466.

Gray, W. M., and R. W. Jacobson, Jr., 1977: Diurnal variation of deep cumulus convection. *Mon. Wea. Rev.,* **105,** 1171–1188.

Greenhut, G. K., 1978: Correlations between rainfall and sea surface temperature during GATE. *J. Phys. Oceanogr.,* **8,** 1135–1139.

Hamilton, K., 1981a: A note on the observed diurnal and semidiurnal rainfall variations. *J. Geophys. Res.,* **86,** 12 122–12 126.

——, 1981b: Latent heat release as a possible forcing mechanism for atmospheric tides. *Mon. Wea. Rev.,* **109,** 3–17.

Harshvardhan, R. Davies, D. A. Randall and T. G. Corsetti, 1987: A fast radiation parameterization for general circulation models. *J. Geophys. Res.,* **92,** 1009–1016.

——, D. A. Randall, T. G. Corsetti and D. A. Dazlich, 1989: Earth radiation budget and cloudiness simulations with a general circulation model. *J. Atmos. Sci.,* **46,** 1922–1942.

Hartmann, D. L., and E. E. Recker, 1986: Diurnal variation of outgoing longwave radiation in the tropics. *J. Climate Appl. Meteor.,* **25,** 800–812.

Hastenrath, S. L., 1967: Diurnal fluctuations of the atmospheric moisture flux in the Caribbean and Gulf of Mexico area. *J. Geophys. Res.,* **72,** 4119–4130.

Haurwitz, B., 1965: The diurnal surface pressure oscillation. *Arch. Meteorol. Geophys. Bioklimatol.,* **A14,** 361–379.

——, and A. D. Cowley, 1973: The diurnal and semidiurnal barometric oscillations, global distribution, and annual variation. *Pure Appl. Geophys.,* **102,** 193–222.

Holton, J. R., 1967: The diurnal boundary layer wind oscillation above sloping terrain. *Tellus,* **19,** 199–205.

Hsu, H.-H., and B. J. Hoskins, 1989: Tidal fluctuations as seen in ECMWF data. *Quart. J. Roy. Meteor. Soc.,* **115,** 247–264.

Hudlow, M. D., 1970: Weather radar investigations on the BOMEX. Research and Development Rept. ECOM-3320, U.S. Army Electronics Command, Fort Monmouth, N.J., 106 pp.

Hunt, B., and S. Manabe, 1968: An investigation of thermal tidal oscillations in the earth's atmosphere using a general circulation model. *Mon. Wea. Rev.,* **96,** 753–766.

Jaeger, J., 1976: Monatskarten des Niederschlags fur die ganze Erde. *Ber. Dtsch. Welterdienstes,* **18**(39), 38 pp plus 13 plates.

Keenan, T. D., J. McBride, G. Holland, N. Davidson and B. Gunn, 1989: Diurnal variations during the Australian Monsoon Experiment (AMEX) Phase II. *Mon. Wea. Rev.,* **117,** 2535–2552.

Kousky, V. E., 1980: Diurnal rainfall variation in Northeast Brazil. *Mon. Wea. Rev.,* **108,** 488–498.

Kraus, E. B., 1963: The diurnal precipitation change over the sea. *J. Atmos. Sci.,* **20,** 551–556.

Liebmann, B., and A. Gruber, 1988: The annual variation of the diurnal cycle of outgoing longwave radiation. *Mon. Wea. Rev.,* **116,** 1659–1670.

Lindzen, R. S., 1978: Effect of daily variations of cumulonimbus activity on the atmospheric semidiurnal tide. *Mon. Wea. Rev.,* **106,** 526–533.

Malkus, J. S., 1964: Convective processes in the tropics. *Proc. Symp. on Tropical Meteorlogy,* Rotorua, New Zealand, 247–277.

McBride, J. L., and W. M. Gray, 1980: Mass divergence in tropical weather systems. Paper I: Diurnal variation. *Quart. J. Roy. Meteor. Soc.,* **106,** 501–516.

McGarry, M., M., and R. J. Reed, 1978: Diurnal variations in convective activity and precipitation during Phases II and III of GATE. *Mon. Wea. Rev.,* **106,** 101–113.

Meisner, B. N., and P. A. Arkin, 1987: Spatial and annual variations in the diurnal cycle of large-scale tropical convective cloudiness and precipitation. *Mon. Wea. Rev.,* **115,** 2009–2032.

Minnis, P., and E. F. Harrison, 1984a: Diurnal variability of regional cloud and clear-sky radiative parameters derived from GOES data. Part I: Analysis Method. *J. Climate Appl. Meteor.,* **23,** 993–1051.

——, and ——, 1984b: Diurnal variability of regional cloud and clear-sky radiative parameters derived from GOES data. Part II: November 1978 cloud distributions. *J. Climate Appl. Meteor.,* **23,** 1012–1011.

——, and ——, 1984c: Diurnal variability of regional cloud and clear-sky radiative parameters derived from GOES data. Part III: November 1978 radiative parameters. *J. Climate Appl. Meteor.,* **23,** 1032–1051.

Mintz, Y., 1984: The Sensitivity of numerically simulated climates to land surface boundary conditions. *The Global Climate,* J. T. Houghton Ed., Cambridge University Press, 70–105.

——, and V. Serafini, 1983: Monthly normal global fields of soil moisture and land surface evapotranspiration. *Symp. on Variations in the Global Water Budget,* Oxford, England, 1981.

Miyakoda, K., 1989: Atmospheric forecast model data assimilation and air–sea flux computations. Atmospheric Forcing of Ocean Circulation, Institute of Naval Oceanography Report 89-1, 56–93.

Murakami, M., 1983: Analysis of the deep convective activity over the Western Pacific and Southeast Asia. Part I: Diurnal variation. *J. Meteorol. Soc. Jpn.,* **61,** 60–75.

Nitta, T., and S. Esbensen, 1974: Diurnal variations in the western Atlantic trades. *J. Meteorol. Soc. Jpn.,* **52,** 254–257.

Ostapoff, F., and S. Worthem, 1974: The intradiurnal temperature variation in the upper ocean layer. *J. Phys. Oceanogr.,* **4,** 601–612.

Price, J. F., and R. A. Weller, 1986: Diurnal cycling: observations and models of the upper ocean response to diurnal heating, cooling, and wind mixing. *J. Geophys. Res.,* **91,** 8411–8427.

Randall, D. A., J. A. Abeles and T. G. Corsetti, 1985: Seasonal simulations of the planetary boundary layer and boundary layer stratocumulus clouds with a general circulation model. *J. Atmos. Sci.,* **42,** 641–676.

——, Harshvardhan, D. A. Dazlich and T. G. Corsetti, 1989: Interactions among radiation, convection, and large-scale dynamics in a general circulation model. *J. Atmos. Sci.,* **46,** 1943–1970.

Rasmusson, E. M., 1967: Atmospheric water vapor transport and the hydrology of North America: Part I, characteristics of the water vapor flux field. *Mon. Wea. Rev.,* **95,** 403–426.

——, 1968: Atmospheric water vapor transport and the water balance of North America: Part II, large-scale water balance investigations. *Mon. Wea. Rev.,* **96,** 720–734.

Reed, R. J., and R. M. Lewis, 1980: Response of upper ocean temperatures to diurnal and synoptic-scale variations of meterological parameters in the GATE B-scale area. *Deep Sea Res.,* **26,** 99–114.

——, and K. D. Jaffe, 1981: Diurnal variation of summer convection over West Africa and the tropical eastern Atlantic during 1974 and 1978. *Mon. Wea. Rev.,* **109,** 2527–2534.

——, D. C. Norquist and E. E. Recker, 1977: The structure and properties of African wave disturbances as observed during Phase III of GATE. *Mon. Wea. Rev.,* **105,** 317–333.

Roll, H. U., 1965: *Physics of the Marine Atmosphere.* Academic Press, 426 pp.

Sellers, W. D., 1965: *Physical Climatology.* The University of Chicago Press, 272 pp.

Short, D. A., and J. M. Wallace, 1980: Satellite-inferred morning to evening cloudiness changes. *Mon. Wea. Rev.,* **108,** 1160–1169.

Sieberg, M., 1961: Atmospheric Tides. *Advances in Geophysics,* Vol. 7, Academic Press, 105–187.

Silva Dias, P. L., J. P. Bonatti and V. E. Kousky, 1987: Diurnally forced tropical tropospheric circulation over South America. *Mon. Wea. Rev.*, **115,** 1465–1478.

Slingo, A., R. C. Wilderspin and S. J. Brentnall, 1987: Simulation of the diurnal cycle of outgoing longwave radiation with an atmospheric GCM. *Mon. Wea. Rev.*, **115,** 1451–1457.

Susskind, J., D. Reuter and M. T. Chahine, 1987: Cloud fields retrieved from analysis of HIRS2/MSU sounding data. *J. Geophys. Res.*, **92D,** 4035–4050.

Tokioka, T., and I. Yagai, 1987: Atmospheric tides appearing in a global atmospheric general circulation model. *J. Meteorol. Soc. Jpn.*, **65,** 423–437.

Wallace, J. M., 1975: Diurnal variations in precipitation and thunderstorm frequency over the coterminous United States. *Mon. Wea. Rev.*, **103,** 406–419.

——, and F. R. Hartranft, 1969: Diurnal wind variations, surface to 30 kilometers. *Mon. Wea. Rev.*, **97,** 446–455.

——, and P. V. Hobbs, 1977: *Atmospheric Science: An Introductory Survey.* Academic Press, 467 pp.

——, and Tadd, R. F., 1974: Some further results concerning the vertical structure of atmospheric tidal motions within the lowest 30 kilometers. *Mon. Wea. Rev.*, **102,** 795–803.

Warren, S. G., C. J. Hahn, J. London, R. M. Chervin and R. L. Jenne, 1986: Global distribution of total cloud cover and cloud-type amounts over land. NCAR/TN-273+STR, 29 pp. and 199 maps.

Washington, W. M., and G. A. Meehl, 1989: Climate sensitivity due to increased CO_2: experiments with a coupled atmosphere and ocean general circulation model. *Climate Dyn.*, **4,** 1–38.

Yagai, I., 1989: Nonmigrating thermal tides detected in data analysis and a general circulation model simulation. *J. Geophys. Res.*, **94,** 6341–6356.

Zwiers, F., and K. Hamilton, 1986: Simulation of solar tides in the Canadian Climate Centre general circulation model. *J. Geophys. Res.*, **91D,** 11 877–11 896.